NTNU

Norwegian University
of Science and Technology

Department of Energy
and Process Engineering

EPT-M-2011-102

MASTER THESIS

for

Peter Joachim Gogstad
Fall 2011

Hydraulic design of Francis turbine exposed to sediment erosion
Hydraulisk design av Francisturbin utsatt for sanderosjon

Background

Sediment erosion in Francis turbines is a large problem for river power plants near the Himalayas and the Andes Mountains. Due to high sediment concentration in the rivers the turbine components are exposed to erosion wear and must be maintained often. During monsoon periods, the sediment concentration is at its highest and the turbines are stopped to reduce the damage on the components. The turbines at La Higuera Power Plant in Chile are a good example on how the sediment erosion effects the power plant operation. These turbines need to be maintained annually due to high erosion wear. This result in a reduction of power production and high maintenance cost. On top of this, the original design has some mechanical design problems. It is therefore of interest to design a new Francis runner, guide vanes and head covers which are more resistant to sediment erosion and have a good mechanical design. A cooperation between SN-Power and NTNU has started and aim to find alternatives for the Francis turbines at La Higuera Power Plant.

Objective

The aim is to carry out a new hydraulic design of runner and guide vanes of the existing Francis turbine at La Higuera Power Plant where the velocity components are reduced.

The following tasks are to be considered:

1. Literature survey
   a. Erosion in Francis turbines
2. Software knowledge
   a. Get familiar with the Francis turbine optimization tool developed at NTNU
   b. Get familiar with the CFD-tool; Ansys CFX
   c. Get familiar with the CAD-tool; Pro-Engineer
3. The student has to learn how Ansys CFX and the optimization tools within Matlab will be used for the parametric study of the Francis turbine design.
4. Design runner and guide vanes using Francis turbine optimization tool. (Modifications of the Francis turbine optimization tool if needed.)
5. 3D-drawings of runner, guide vanes and head covers
6. Parametric study of the turbine design by using the Francis turbine optimization tool and CFD-analysis where the aim is to reduce the sediment erosion of the guide vanes and runner.

Within 14 days of receiving the written text on the master thesis, the candidate shall submit a research plan for his project to the department.

When the thesis is evaluated, emphasis is put on processing of the results, and that they are presented in tabular and/or graphic form in a clear manner, and that they are analyzed carefully.

The thesis should be formulated as a research report with summary both in English and Norwegian, conclusion, literature references, table of contents etc. During the preparation of the text, the candidate should make an effort to produce a well-structured and easily readable report. In order to ease the evaluation of the thesis, it is important that the cross-references are correct. In the making of the report, strong emphasis should be placed on both a thorough discussion of the results and an orderly presentation.

The candidate is requested to initiate and keep close contact with his/her academic supervisor(s) throughout the working period. The candidate must follow the rules and regulations of NTNU as well as passive directions given by the Department of Energy and Process Engineering.

Risk assessment of the candidate's work shall be carried out according to the department's procedures. The risk assessment must be documented and included as part of the final report. Events related to the candidate's work adversely affecting the health, safety or security, must be documented and included as part of the final report.

Pursuant to "Regulations concerning the supplementary provisions to the technology study program/Master of Science" at NTNU §20, the Department reserves the permission to utilize all the results and data for teaching and research purposes as well as in future publications.

The final report is to be submitted digitally in DAIM. An executive summary of the thesis including title, student's name, supervisor's name, year, department name, and NTNU's logo and name, shall be submitted to the department as a separate pdf file. Based on an agreement with the supervisor, the final report and other material and documents may be given to the supervisor in digital format.

Department of Energy and Process Engineering, 22. August 2011

Olav Bolland
Department Head

Prof. Ole G. Dahlhaug
Academic Supervisor

Research Advisors: Per Egil Skåre, DynaVec

Preface

This master thesis has been written at the Waterpower Laboratory, Department of Energy and Process Engineering at the Norwegian University of Science and Technology (NTNU) during autumn 2011. And finally it is finished a wet winter day in Trondheim.

I would like thank my supervisor Ole Gunnar Dahlhaug for introducing me to the field of Francis design. It has been very interesting, sometimes frustrating, but he has always shared of his great knowledge and inspired me to continue. Unfortunately time has passed to fast for me to explore all the ideas I have got.

I would also thank Mette Eltvik, Bjørn Winther Solemslie and Martin Holst for some good discussion and help you have provided.

I special thanks goes to Kristine Gjøsæter for introducing me to the design software Khoj, answering silly questions, finding the small errors which I had spent hours not understanding and to not forget all the good discussions.

My sincere thanks go to my fellow students at Waterpower Laboratory for all good discussions and great working environment. Some have made me laugh, some have inspired me, some have given me help but you have all given me memorable moments.

A great time as student has past. I already miss it!

Peter Joachim Gogstad
Trondheim, January 15, 2012

Abstract

High concentrations of sediments is a serious problem for hydropower stations in the Himalayas and the Andes Mountains. For run-of-river power plants sediment causes heavy erosion even with settling basins. This leads to reduced operating hours and high maintenance cost. In addition, the original design experienced problem with heavy cavitation.

The objective of this master thesis is to carry out new hydraulic design of the runner and guide vanes of the existing Francis turbines in La Higuera Power Plant with reduced velocity components. To achieve this the cause of the heavy cavitation, which made the turbine fail, has to be established.

Results from numerical simulations indicates a low pressure zone causing heavy leading edge cavitation is the reason for the turbine failure. The off-design operation has made the cavitation even worse.

To carry out a new design, the in-house design software Khoj was used. Some new parameters, like blade leaning, were included in the program. Blade leaning is an important tool for pressure balancing the runner blade. Further, a parameter study was carried out to investigate the effect of blade leaning, blade angle distribution and blade length.

The numerical simulation indicates proper pressure balancing could have avoided the cavitation problems and a new design should have an X-blade shape. Because the power plant is already built, the number of variables is limited. The rotational speed, inlet and outlet diameter remained constant. This made it impossible to significantly reduce the relative velocities. Therefore, coating of all wet surfaces is proposed to reduce the effect of erosion.

The main objective for this thesis has been to identify the cause of the turbine failure and develop a new design to fit in the existing power plant. Complete 3D-drawings of the design, including runner and guide vanes, has not been made due to lack of time.

Sammendrag

Høye konsenstrasjoner av harde mineraler er stor utfordring for vannkraftverk i Sør-Amerika og Himalaya. Elvekraftverk er spesielt utsatt for sanderosjon. Slitasje fra sanderosjon fører til redusert virkningsgrad og økt vedlikehold som igjen reduserer antall driftstimer.

Denne masteroppgaven har som mål å komme opp med et nytt design for turbinehjulet i vannkraftverket La Higuera i Chile. Det eksisterende turbinhjulet ble ødelagt på grunn av kraftig kavitasjon tidligere i år. Det er ønskelig at det nye designet har lavere relative hastigheter for å redusere erosjonen, samtidig må årsaken til kavitasjon fjernes.

Resultater fra numeriske simuleringer indikerer en lavtrykkssone på sugesiden av bladet like ved innløpet. En slik lavtrykkssone skaper kraftig kavitasjon og det er derfor antatt at den er årsaken til kavitasjonen som ødela turbinen. Drift utenfor bestpunkt har gjort kavitasjon enda verre.

Design programmet Khoj, som er utviklet ved Vannkraftlaboratoriet, ble brukt til lage nye design. Ulike design ble brukt for en parameterstudie. Khoj er også blitt viderutviklet som en del av oppgaven og noen nye parametere er blitt inkludert. Den viktigste forbedringen er muligheten for å trykkbalansere løpehjulsbladet.

De numeriske simuleringene indikerer at ved å trykkbalansere bladet vil det være mulig å unngå kavitasjon. Trykkbalanseringen indikerer videre at det nye bladet bør få et såkalt X-blad-design. Ettersom La Higuera allerede er bygget, er det et begrenset antallvariabler. Rotatsjonshastigheten, innløp- og utløps-diameteren er holdt konstant fordi det har vært ønskelig å beholde generator og ledeskovler. Dette har imidlertid gjort det umulig å redusere de relative hastigheten betydelig. Derfor anbefales det coating for alle "våte overflater".

Hovedfokuset i oppgaven har vært å finne årsaken til hvorfor turbinene i La Higuera er blitt ødelagt og designe en ny turbin som passer i det eksisterende vannkraftverket. Det har derfor ikke vært tid til å lage fullstendige 3D-tegninger for ny turbin med ledskovler.

Contents

1 Introduction **1**
- 1.1 Hydro power in South America . . . 1
- 1.2 La Higuera . . . 1
- 1.3 Objective . . . 2
- 1.4 Outline . . . 2

2 Background **3**
- 2.1 Previous Work . . . 3
  - 2.1.1 The design software . . . 4

3 Wear **5**
- 3.1 Wear mechanisms . . . 5
- 3.2 Abrasive wear . . . 5
- 3.3 Erosive wear . . . 6
  - 3.3.1 Wear mechanisms . . . 7
- 3.4 Cavitation . . . 8
  - 3.4.1 Cavitation areas . . . 10
- 3.5 Erosion areas in Francis turbines . . . 10
  - 3.5.1 Stay vanes . . . 10
  - 3.5.2 Guide vanes . . . 11
  - 3.5.3 Runner . . . 12
- 3.6 Erosion classifications . . . 13
- 3.7 Erosion models . . . 13
- 3.8 Design measures to decrease erosion . . . 14

4 Francis Turbine Design **17**
- 4.1 Blade Thickness . . . 17
- 4.2 Blade leaning . . . 19

5 Design Procedure **21**
- 5.1 New features of the program . . . 21
  - 5.1.1 Visual changes . . . 21
  - 5.1.2 Main dimensions . . . 21
  - 5.1.3 Leading and trailing edge geometry . . . 21
  - 5.1.4 Blade leaning . . . 23
  - 5.1.5 Guide vanes . . . 24
  - 5.1.6 Blade thickness . . . 25

6 CFD Theory **27**
- 6.1 Grid properties . . . 27
- 6.2 Mesh Generation . . . 27
- 6.3 Turbulence Modelling . . . 27

7 Computational Model for Francis Turbine **31**
- 7.1 Mesh generation . . . 31

7.2 Boundary conditions 31

8 Reference Design **35**
8.1 CFD Analysis 35

9 Verification **41**
9.1 Multilevel CFD 41
9.2 Coarse mesh 43

10 Results **45**
10.1 La Higuera 45
10.2 Parameter Study 46
10.3 Design H0 46
10.4 Single parameter studies 48
10.4.1 Effects of blade leaning 48
10.4.2 Increasing blade length 50
10.4.3 Effects of changing blade angle distribution 51

11 Discussion **55**
11.1 Blade leaning 55
11.2 Weaknesses in Khoj 56

12 Conclusion **59**

13 Further Work **61**

A Background information on the design sofware **I**

B CFD **XXIII**
B.1 Basic equations XXIII

C View of Khoj **XXV**

List of Figures

3.1 Mechanisms of abrasive wear [1] 5
3.2 Mechanisms of erosive wear [1] 7
3.3 Main types of cavitation in Francis turbines: (a) leading edge cavitation, (b) travelling bubble cavitation, (c) draft tube swirl and (d) inter-blade vortex cavitation [2] 9
3.4 Cavitation areas in runner [3] 10
3.5 Areas Exposed to sediment erosion wear [4] 11
3.6 Design of stay vane inlet [4] 11
3.7 Secondary flows, leakage flows and horse shoe vorticies on guide vanes [4] 12
3.8 Illustration of particle flow separation at high acceleration [5] 12
4.9 Load model of the blade between hub and shroud [4] 17
4.10 Definition of a, b, Δr and R_M [4] 18
4.11 Tokke turbine without blade leaning [6] 20
4.12 Different blade leaning at Cahua hydropower plant [6] 20
5.13 Current design procedure. The red ring indicates the working area of this thesis 22
5.14 Shape of leading and trailing edge [4] 23
5.15 Blade with blade leaning option 1 23
5.16 Blade with blade leaning option 2 24
6.17 SST model [4] 28
6.18 Wall function. Adapted from [7] 29
7.19 TurbiGrid ATM mesh 32
7.20 Computational domain 33
8.21 y^+-values on the runner blade formesh with *Factor ratio = 1.1* . . . 37
8.22 Streamlines in draft tube at BEP 37
8.23 Relative velocity in runner seen from outlet and from top 38
8.24 Static pressure on the blade, reference mesh 38
8.25 Pressure distribution between blades 38
8.26 Trailing edge shape in Turbogrid, somewhat exaggerated [4] 39
9.27 Static pressure on the blade, reference mesh 42
9.28 Static pressure on the blade, mesh A 42
9.29 Comparison of draft tube velocities 43
9.30 Static pressure on the blade, viscous simulation results 43
9.31 Static pressure on the blade, inviscid simulation results 44
10.32 Comparison of the suction side for the reference blade at different heads 45
10.33 Efficiency as a function of head for different mesh 45
10.34 Pressure distribution on the blade for design H0 47
10.35 Pressure distribution between blades 47
10.36 Draft tube velocities at BEP for the H0 design 48
10.37 Comparisson of different blade leaning 49
10.38 Pressure distribution between blades for BL1 50
10.39 Static pressure on the blade for TE2 51

10.40Pressure distribution between blades for TE2 51
10.41Different shapes of the blade angle distribution [4] 52
10.42Static pressure on the blade for Shape 1 53
10.43Streamlines in draft tube at BEP for Shape 2 53
C.1 Tab 5 - Radial view of runner blade. The new blade leaning parameter is visible in the upper left corner. The graphs in the center displays change in energy distribution when blade leaning is introduced. XXV
C.2 Tab 6 - Blade thickness. In the upper left corner, the blade thickness distribution is displayed. At the bottom, the trailing and leading edge shape is displayed XXVI
C.3 Tab 8 - Guide Vanes. This tab displays the runner cascade in 2D. Tha shape of the leading edge is shown in the figure to the left. The different parameters are sorted XXVII
C.4 Tab 9 - Runner cascade. Currently this tab i displaying the runner, guide vanes and stay vanes for La Higuera. It will be developed to show the runner cascade in 3D XXVII

List of Tables

3.1 Measures to decrease erosion [8] 14
7.2 Boundary layer refinement control data 31
8.3 Reference Turbine Data 35
8.4 Reference Turbine Mesh Data 36
8.5 Design software data and reference turbine data 36
9.6 Mesh information 41
9.7 Mesh information 43
10.8 Comparison of H0 design and the reference design, both inviscid simulation and coarse mesh 46
10.9 Parameters for single effects study 48
10.10Comparison of H0 design and the reference design, both inviscid simulation and coarse mesh 49
10.11Comparison of H0 design and the reference design, both inviscid simulation and coarse mesh 50
10.12Comparison of H0 design and different blade angle distribution . . . 52

Nomenclature

Symbols

Symbol	Description	Unit
a	Difference between inlet and outlet radius of runner	m
A	Area	m^2
B	Height	m
b	Height of shroud	$-$
C	Absolute velocity	m/s
d	Diameter	m
D	Diameter	m
E	Specific hydraulic energy	J/kg
F	Force	N
g	Acceleration of gravity	m/s^2
G	Length of streamline in axial direction	m
H	Length of streamline in radial direction	m
h	Relative head	$-$
H_e	Head	m
i	Factor that relate erosion rate and velocity	$-$
I	Second area moment of inertia	m^4
K	Constant	$-$
k_{ol}	Overlap factor	%
k	conduction factor	
L	Length	m
m	Mass	kg
M	Bending moment	Nm
N	Number of measurements	m
n	Rotational speed	rpm
p	Pressure	Pa
P	Power	W
q	Relative volume flow	$-$
Q	Flow rate	m^3/s
r	Radius	m
R	Radius	m
Re	Reynolds number	$-$
V	Volume	m^3
U	Peripheral velocity	m/s
W	Relative velocity	m/s
y^+	Non-dimensional distance	$-$
Z	Number of items	m

Greek Symbols

Symbol	Description	Unit
α	Guide vane angle	$^\circ$
β	Blade angle	$^\circ$
η	Efficiency	$-$
λ	Turbine coefficient	$-$
ϕ	Angle in spiral casing cross section	$^\circ$
π	Constant	$-$
μ	Dynamic viscosity	$kg/(m{\cdot}s)$
ρ	Density	kg/m^3
σ	Bending stress	MPa
τ_w	Wall shear stress	Pa
θ	Angle in the radial view	$^\circ$
ω	Angular velocity	rad/s
Ω	Speed number	$-$

Sub-symbols

$*$	Refers to best efficiency point of turbine
amb	Refers to ambient
dyn	Refers to dynamic
e	Refers to effective
f	Refers to friction
h	Refers to hydraulic
loc	Refers to local
m	Refers to measured static pressure
R	Refers to rated
SE	Refers to sudden expansion
$stat$	Refers to static
gv	Refers to guide vane
gvi	Refers to guide vane inlet
gvo	Refers to guide vane outlet
h	Refers to hydraulic
m	Refers to meridional direction
max	Refers to maximum value
min	Refers to minimum value
r	Refers to runner
sv	Refers to stay vane
svi	Refers to stay vane inlet
svo	Refers to stay vane outlet
u	Refers to peripheral direction
1	Refers to inlet of turbine runner
2	Refers to outlet of turbine runner
$\underline{\chi}$	Underline refers to reduced value

Abbreviations

BEP	Best Efficiency Point
CFD	Computational Fluid Dynamics
FEM	Finite Element Method
FSI	Fluid Structure Interaction
GUI	Graphical User Interface
IEC	International Electrotechnical Commission
NPSH	Net Positive Suction Head
NTNU	Norewgian University of Science and Technology
rpm	Revolutions per minute
SST	Shear Stress Transport

1 Introduction

1.1 Hydro power in South America

The Andes Mountains is the world's longest mountain range, stretching 9000 km from Patagonia in south to Columbia in north. The nature forces erodes the mountains and transports sediments down the rivers. The run-of-river power plants experience large problems with high sediment concentration in the river. Without massive dams, the have to use settling basins which only reduces the sediment concentration. As the hard mineral quartz is common in the Andes, the turbines suffer severe erosion damage.

SN Power has invested in power plants both in Peru and Chile. The Cahua Power Plant in Peru has earlier been the subject for a master thesis at the Waterpower Laboratory. In Chile, the potetial hydropower is about 24,000 MW, but SN Power has only utilized fraction [9]. As a lot of the potetial rivers are far from the consumption area, the building of a power plant also include large power lines. This cause destruction of the wilderness and possibly removal of native people. The last years, the focus to preserve the nature has increased and causes problems for massive development. Developers are therefore often restricted to use run-of-river power plants as they have less impact on the nature.

The power plant managers would like to transfer as much energy as feasible to the grid and high efficiency is therefore important. However, they experience frequent shut-down of the power plant as the sediment erosion causes damage and time is needed to repair. The efficiency decreases with the erosion damage and hence the profit. Therefore, a solution to the sediment problem is an important task in these countries.

La Higuera Power plant is located beside Tinguiririca River in the O'Higgins region in Chile. The power plant is owned by Tinguiririca Energia, which again is partly owned by SN Power. The run-of-river hydropower plant La Higuera is equipped with two Francis turbines, each with nominal output of 77.5 MW.

1.2 La Higuera

La Higuera Power Plant in the Chilean Andes recently started operation. However, due to mechanical design problems both turbines have failed. During a visit August 16th 2011, Ole Gunnar Dahlhaug inspected the one unit which was still operating and found cavitation in large parts of the operating range. Heavy cavitation due to operation at a higher head than designed head is assumed to have caused the failure. SN-Power in co-operation with NTNU will work to design a new runner and guide vanes to fit in the existing power station.

In addition the power plant has problems with sediment erosion. Due to high sediment concentration in the rivers the turbines are exposed to erosion wear and

need extra maintenance. A second goal for the new design would be to reduce the sediment erosion wear of the runner and guide vanes.

An in-house Francis turbine design tool, Khoj, has been developed in Matlab. This program will be modified to produce a new runner and guide vanes within the limitations of the power plant.

1.3 Objective

The objective is to carry out a new design of runner and guide vanes for the existing Francis turbine with reduced velocities for La Higuera Power Plant. Matlab will be used to generate the runner geometry and for a first stage of optimization. Further, a parametric study will be carried out by using both Khoj and CFX iteratively.

1.4 Outline

The thesis will give a brief background for the thesis in chapter two, before presenting relevant theory in chapter three. All relevant design theory behind the program is presented in Appendix A, while relevant design theory for the improvements is presented in chapter four. Chapter six and seven gives a relevant overview concerning CFD analysis and setup. A new turbine design for La Higuera with reduced sediment erosion wear will be proposed. A reference design generated using the design software and analyzed in CFD is presented in chapter eight. Furher follows the parameter study with CFD results, discussion of the results and conclusion

2 Background

2.1 Previous Work

Sediment erosion is a well documented field and lot of papers and books have been published. However, only a few publications focus on sediment erosion in hydraulic machinery. Litterature about Francis turbine design is harder to retrieve as it is based on experience and subject to copyright. However, pump impeller design is well described in the litterature and applies similar methods as for Francis turbine design.

Former NTNU professor Hermod Brekke, has been and still is one of most influential people in the hydropower industry [10]. He has performed a significant amount of research concerning sediment erosion in hydraulic machinery, including design and material properties and development of sediment erosion resistant coatings.

During the last couple of years, the Waterpower Laboratory has increased its focus on sediment erosion. This has given the opportunity for several project, master and doctoral theses. In 2004, Jonas Jessen Ruud wrote his master thesis on *Sediment handling problems at Jhimruk Power Plant.* Same year, Bhola Thapa finished his doctoral thesis Sand Erosion in Hydraulic Machinery.

Mattias Rögner started th procedure of proposing a new Francis turbine design with reduced velocity components in 2008. This has been continued by Hallvard Meland in 2010.

In 2008, Ola Gjømle Thorvaldsen performed a CFD and stress analysis of the Francis turbine of Cahua power plant in Peru. Mette Eltvik used Cahua power plant as a reference case for her project and master thesis in 2010. The CFD analysis with two-phase fluid particle flow she performed was compared with the erosion damage on the old turbines of Cahua. Eltvik has continued the CFD studies of sediment erosion in her on-going PhD.

Hari Prasad Neopane finished his doctoral thesis *Sand Erosion in Hydro Turbines* in 2010. His thesis included experimental tests, CFD analysis (two-phase fluid particles) and field studies of sediment erosion. Both doctoral theses of Neopane and Thapa are considered to be important contributions to the research field of sediment erosion in hydraulic machinery.

In 2011, Kristine Gjøsæter finished her master thesis *Hydraulic Design of Francis Turbine Exposed to Sediment Erosion.* She developed the MATLAB design sofware, Khoj, through both her project and master thesis and performed CFD analyses on different design for a new turbine to Jhimruk hydropower plant in Nepal. Gjøsæter was a part of the Francis turbine design team of spring 2011 also including Biraj Singh Thapa (*Hydraulic design of Francis turbine exposed to sediment erosion*), Helene P. Erichsen (Mechanical design of Francis turbine exposed to sediment erosion) and ph.d candidate Mette Eltvik.

2.1.1 The design software

The design software, Khoj, is an in-house developed Francis turbine design software. It has been developed by Kristine Gjøsæter as a part of her project and master thesis. The software is programmed in Matlab with graphical user interface (GUI). Tabs allow for easy access to the different steps of the turbine design. The program will automatically update the chosen tab, if previous data has been altered.

The software has been further developed in co-operation with Kristine Gjøsæter as a part of this thesis. The development is described in detail in Chapter 5. The background information behind the design software can be found in Appendix A.

3 Wear

Damages in hydro power turbines are mainly caused by cavitation problems, sand erosion, material defects and fatigue [11]. This chapter will give an overview of the wear mechanism which includes cavitation and sand erosion. Material defects will be briefly mentioned as a cause of different wear mechanisms.

3.1 Wear mechanisms

In material science, wear is a collective term for the different mechanisms which cause deformation or displacement of solids. In general, the wear mechanisms can be classified in three categories; mechanical, chemical and thermal actions [1]. Mechanical wear will be the main focus for this chapter as it is the mechanical wear which is affected by volume flow through the turbine.

Further, Stachowiak and Batchelor [1] classifies three types of mechanical wear; abrasive, erosive and cavitation wear. Abrasive and erosive are due to particles on the fluid flow, while cavitation is caused by the collapse of bubbles on the surface. Abrasive wear is defined as the loss of material by the passage of hard particles over a surface. Erosive wear is caused by the impact of particles against a solid surface.

3.2 Abrasive wear

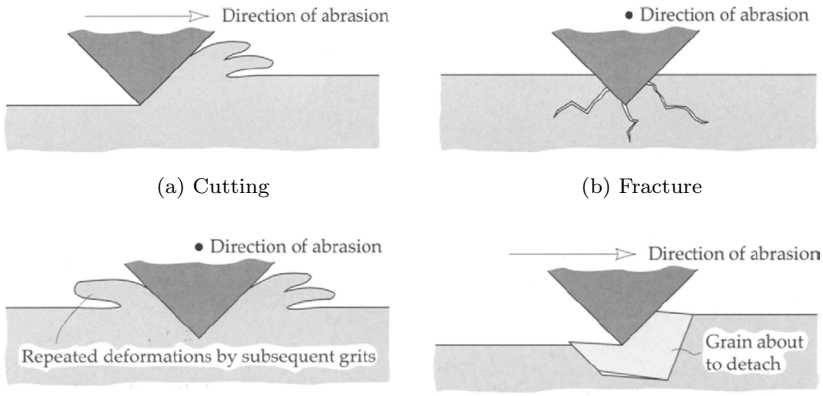

(a) Cutting

(b) Fracture

(c) Fatigue by repeated ploughing

(d) Grain pull-out

Figure 3.1: Mechanisms of abrasive wear [1]

Abrasive wear occurs when particles of a material with equal or greater hardness than the solid surface interacts [1]. The different mechanisms are illustrated in Figure 3.1.

Cutting occurs when a sharp grit strikes a softer surface and material can be removed as wear debris. The cutting mechanism is illustrated illustrated in Figure 3.1a. For surfaces of brittle material, fractures or cracking may occur as illustrated in Figure 3.1b.

The accumulation of cracks over time may result large debris removed from the surface. For ductile materials exposed to blunt grit, cutting is unlikely, but repeated scratching will cause deformation of the surface as illustrated in Figure 3.1c. In this case, removal of debris is the result of metal fatigue. Detachment of grains is illustrated in Figure 3.1d. This form of abrasive wear mainly applies to brittle materials like ceramics due to relatively weak boundary between grains. When present, the entire grain is lost as wear debris leading to rapid reduction of the material [1].

3.3 Erosive wear

Erosive wear is affected by several factors which differentiate the erosion mechanisms and the erosion rate. The factors can be categorized into [1, 12, 13, 5]:

1. Operating conditions - velocity, acceleration. impingement angle, flux rate or concentration, medium of flow and temperature

2. Eroding particles properties - size, shape hardness and material

3. Target material properties - chemistry, elastic property, hardness and surface morphology

The most important factors would be velocity, impingement angle and particle concentration, as these factors occurs in almost every erosion model.

Impingement angle

The impingement angle or impact angle is defined as the angle between the eroded surface and the trajectory of the particle just begfore impact (ref bola). The erosive wear rate is also dependent on the impingement angle for different materials. Ductile materials will have the highest wear rate for impingement angle around 30°, while brittle materials typically have a higher wear rate at high impingement angles like 80-90° [1].

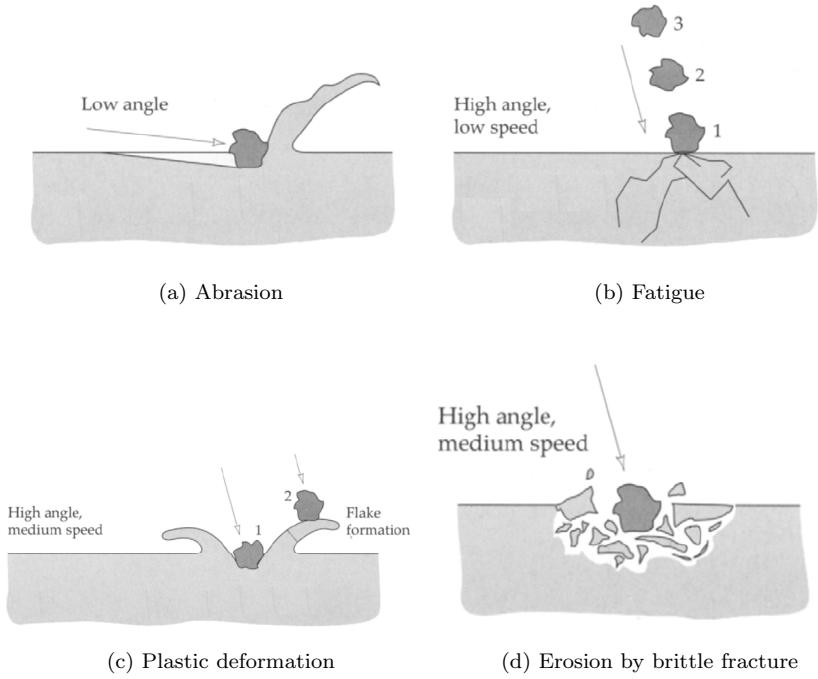

(a) Abrasion

(b) Fatigue

(c) Plastic deformation

(d) Erosion by brittle fracture

Figure 3.2: Mechanisms of erosive wear [1]

3.3.1 Wear mechanisms

The main wear mechanisms are illustrated in Figure 3.2 [1]. A low impact angle, material is removed by a cutting action, similar to abrasive wear, illustrated in Figure 3.2a. For particles with high impingement angle, but low speed, the kinetic energy of the particle is not enough to deform the surface material. However, repeated strikes might cause surface fatigue which is illustrated in Figure 3.2b. For particles with medium velocity and high impact angle, the material property is decisive. For ductile materials, the impacting particles will cause plastic deformation as shown in Figure 3.2c and debris is caused by particles hitting the flakes around the initial striking point. Brittle materials are more exposed to fracture. Fractures are most likely to occur when the surface is hit by sharp particles and debris will detach because of surface cracking as illustrated in Figure 3.2d.

In practice, both plastic deformation and cutting occur at the same time. This is valid above a certain velocity known as the critical velocity. The critical velocity depends both on surface properties and particle properties [5]. Below the critical velocity, the particle will not have enough energy to cut into the surface.

3.4 Cavitation

Cavitation is the development of vapor structures in an originally liquid flow due to pressure drops in the flow itself, and the collapse in high pressure regions [3]. Low pressure zones are well known phenomena in flows and occur i.e. when a flow exits a converging geometry and enters a diverging geometry. The velocity is at maximum at throat where the cross-section is smallest. According to the Bernoulli equation, at the point where the velocity is at its maximum, the pressure is at its minimum and the risk of cavitation is greatest [12]. Cavitation is a local phenomena and only occurs under special conditions and pressure differences are necessary for cavitation to occur [14].

Escaler [2] describes five main types of cavitation:

- Leading edge cavitation
- Travelling bubble cavitation
- Draft tube swirl
- Inter-blade vortex cavitation
- Von Karman vortex cavitation

Leading edge cavitation
Leading edge cavitation takes form of an attached cavity on the suction side of the runner blades due to operation at a higher head than the machine design head when the incidence angle of the inlet flow is positive and largely deviated from the design value (see Figure 3.3(a)). Operation on lower head than design head, the cavitation can occur on the pressure side if the incident angle is negative. If unstable, this type of cavitation is very aggressive and is likely cause sevear damage to the blades and provoke pressure fluctuations [2].

Travelling bubble cavitation
As the fluid moves across from a low pressure zone to higher pressure zones, a cyclic formation and collapse of bubbles is generated. This is what Escaler [2] describes as travelling bubble cavitation (see Figure 3.3(b)). The collapses of bubbles are noisy, but not necessarily harmful unless the bubbles collapse on a surface. When a bubble collapses on a surface, the liquid surrounding the bubble is first accelerated before abruptly decelerated as it collides with the surface. The collision generates large stresses on the surface and transient pressure can reach as high as 1500 MPa [1]. This form of cavitation may reduce the machine efficiency significantly [2].

Draft tube swirl
A low pressure zone in core of the flow is generated due to rotation and centrifugal forces. Hence, vortices are likely to cavitate in the core of the flow [12]. This is what Escaler [2] describes as the draft tube swirl (see Figure 3.3(c)). The swirl may occur both on partial load due to the residual circumferential velocity component of the flow discharged from the runner. The cavitation itself is quite harmless as long as the vapour bubbles do not collapse at a surface. However, strong fluctuations

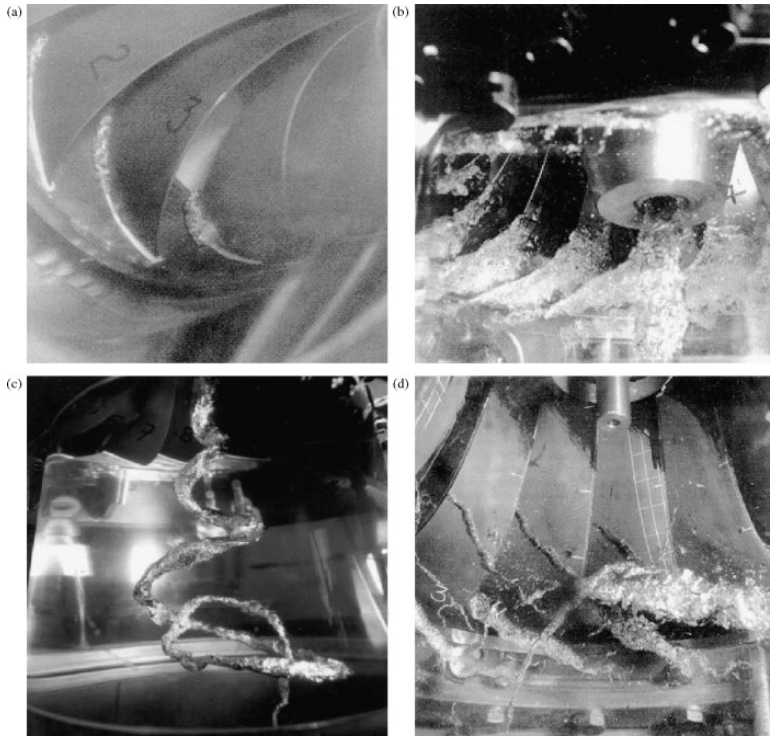

Figure 3.3: Main types of cavitation in Francis turbines: (a) leading edge cavitation, (b) travelling bubble cavitation, (c) draft tube swirl and (d) inter-blade vortex cavitation [2]

may occur if the precession frequency matches one of the free natural oscillation frequencies of the draft tube or penstock. Constructive interference will then provoke large bursts of pressure pulsations in the draft tube, which again causes srong vibrations on the turbine and possibly the powerhouse.

Inter-blade vortex cavitation
Inter-blade vortex cavitation is formed by secondary vortices in the blade channels and is caused by flow separation. The cavitation is usually located in the area of the intersection between leading edge and hub and at the hub between two blades as location D in Figure 3.4. These vortices will only cause erosion damage if their tip is in contact with the runner, but they usually only occur at partial load as illustrated in Figure 3.3(d).

Von Karman vortex cavitation
The last form of cavitation is the Von Karman vortex cavitation. Von Karman vorticies are usually associated with vortex-shedding behind objects. This will also occur in turbines from the trailing edge of the plades. The periodic vortex-shedding may cause severe pulsations and a singing noise and as a result the trailing edge

might be damaged [2]. Traling edges which has curved shape from hub to shroud are more vulnerable to this. Modern turbines therefore usually have a quite straight trailing edge to avoid such damages (ref ole gunnar).

Cavitation wear occurs in several stages. The preliminary stage or incubation period, is without significant mass loss and the surface undergoes mainly plastic deformation. Over time, successive bubble collapses on the material surface leads to fatigue followed by rupture and subsequent material removal [12, 1]. Simultaneous occurrence of cavitation and erosive wear can accelerate the cavitation wear due to synergetic interaction between the two wear mechanisms. For hydraulic turbines in sandy water, the presence of particles will increase the wear rate as the bubble collapsing will cause the particles to hit the surface with high speed [1, 14].

3.4.1 Cavitation areas

While sediment erosion can occur on all wet surfaces, cavitation wear are restricted to the runner and draft tube area because that is where the low pressure zones occur [3].

The areas most exposed to cavitation in the runner is illustrated Figure 3.4. Leading edge cavitation occurs at location (A) and (B), Travelling bubble cavitation usually occurs at location (C) and inter-blades cavitation usually occurs at location (D) [3]. Von Karman vortex cavitation occurs at the trailing edge, but will damage the trailing edge due to pressure pulsations.

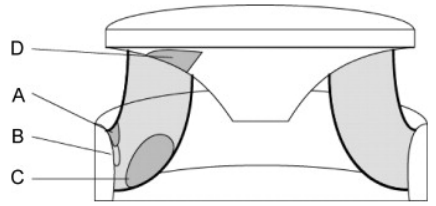

Figure 3.4: Cavitation areas in runner [3]

3.5 Erosion areas in Francis turbines

3.5.1 Stay vanes

Erosion in the at the stay vanes occurs due to secondary flows from the spiral casing influencing flow the angle, and due to the high absolute velocity. The erosion damage is worst close to upper and lower cover [4]. The spiral casing has been modified to reduce the propagation of secondary flows from the spiral casing into stay vanes. Figure 3.6 shows both modern and old design. Reducing the secondary flows, also reduces the erosion damage.

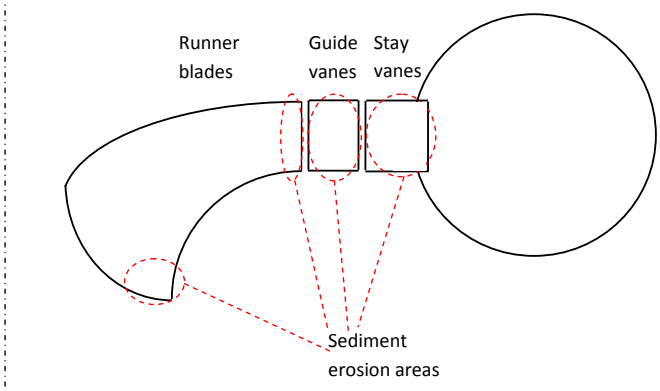

Figure 3.5: Areas Exposed to sediment erosion wear [4]

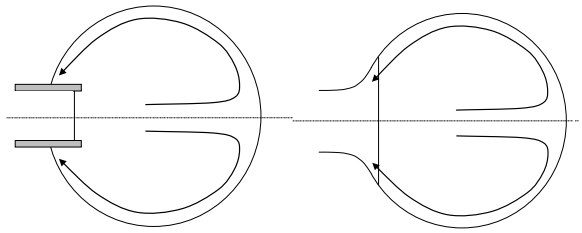

(a) Modern design

(b) Erosion by brittle fracture

Figure 3.6: Design of stay vane inlet [4]

3.5.2 Guide vanes

Duan and Karelin [15] classifies erosion in the guide vanes into four categories:

- *Turbulence erosion* occur in the outlet region as a consequence of high velocities and small particles suspende in the flow. Turbulence erosion can also be found on the facing plates.
- *Secondary flow erosion* occur in corners like between facing plates and guide vanes. The secondary flows are caused by horse shoe vorticies around obstacles like the guide vane inlet as illustrated in Figure 3.7.
- *Leakage erosion* occur due to leakage flow through small gaps between guide vanes and facing plates. The leakage flow, illustrated in Figure 3.7 will also increase the horse vorticies on the suction side of the guide vane due to pressure difference.
- *Acceleration* of the main flow creates an acceleration of sand particles normal to the streamlines. This causes the particles to collide with the guide vane

surface. The impacts of large particles ($d_p < 0.5mm$) will normaly cuase heavy erosion damage.

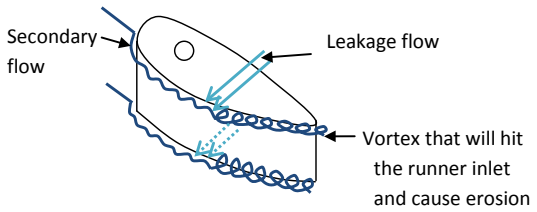

Figure 3.7: Secondary flows, leakage flows and horse shoe vorticies on guide vanes [4]

Thapa [5] states that small particles will ($d_p > 0.5mm$) will follow the streamline s longer than the larger particles due to momentum of the larger particles. Figure 3.8 illustrates this in a Pelton turbine bucket. It is assumed that the same effect might occur in Francis turbines as well.

3.5.3 Runner

Erosion wear at runner is indirectly caused by the guide vanes. Vortices are created at top and bottom of the guide vanes due to leakage flow between the cover and guide vane, as illustrated in Figure 3.7. The vorticies cause erosion at the top and bottom of the leading edge of the runner.

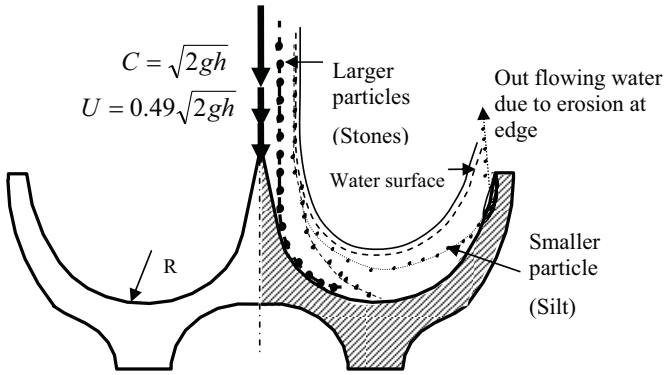

Figure 3.8: Illustration of particle flow separation at high acceleration [5]

The highest relative velocities are found close to the shroud at the runner outlet. They high relative velocity is a cause of turbulence erosion. In addition, if the runner outlet is subject to low pressure, cavitation is also likely to occur. Synergy between both processes can accelerate the wearing process considerably.

3.6 Erosion classifications

Duan and Karelin [15] classifies sediment erosion in hydro turbine into three subcategories.

- *Micro erosion* occur due to small particles ($d_p < 60\mu m$) at high velocities gaining a high rotational velocity in boundary layer turbulence and thus inducing abrasive erosion on the surfaces, especially in the runner outlet region.
- *Secondary flow vortex erosion* occur due to secondary flow in corners and due to horse shoe vortices around obstacles, like the guide vane shafts. This kind of erosion is caused by a combined effect of boundary layers and change of flow acceleration.
- *Acceleration* of large particles ($d_p < 0.5mm$) normal to the streamlines cause the parties to collide with the walls.

Bardal [16] also divides erosion into three subcategories similar to the ones classified by Duan and Karelin.

- *Impingement erosion* occurs for two-phase flows changing flow direction as particles then hit the material surface.
- *Turbulence erosion* occur in areas with strong flow accelerations. This is typically found at the outlet of an inner curve of a bend, and thus also the outlet of a runner close to the shroud
- *Wear and tear* due to particles flowing along and in contact with the surface.

3.7 Erosion models

As mentioned, velocity is included in almost every erosion model. According to Truscott [17], several authors has given a simplified expression to relate erosion rate to velocity and particle properties based on test results. The most used expression is

$$Erosion \propto Velocity^i \tag{3.1}$$

where i i depending on material properties, but usually close to three.

The erosion rate is also assumed to have be proportional to the concentration up to a certain limit. Above this limit the erosion rate is reduced due to interference between arriving and rebounding particles. The relation is usually presented as

$$Erosion \propto Velocity^k \tag{3.2}$$

where k varies between 0.25 and 1.27 depending on material. However, for most materials tested over a longer period of time, k is close to one. Hence, considering erosion rate proportional to concentration is a satisfactory approximation [5].

In general, erosion is a complex process depending on several different variables. As presented earlier in this chapter, erosion can be seen as a function of the operating conditions, particle properties and surface material properties. A general formula for the erosion rate can then be presented as [16]:

$$W = K_{mat} \cdot K_{env} \cdot c \cdot V^i \cdot f(\alpha) \tag{3.3}$$

Where the erosion rate, W, is given as mm/year. K_{mat} is the material constant, K_{env} is the constant describing the enviroment, c is the concentration of particles and $f(\alpha)$ is a function of impingement angle. Other models take more variables into account such as Tabakoff's model and Bergeron's model.

3.8 Design measures to decrease erosion

It is an goal to reduce the erosion in turbines as it leads to reduced damage and decreased maintenance cost. The last 15 years significant reduction of thickness of runner blades, hub and shroud has been observed to increase efficiency [18]. The material strength has remained unchanged, leaving the turbine more vulnerable for stresses and erosion. The measures to decrease erosion presented in Table 3.1 will possibly affect the turbine negative on other aspects.

Measure	**Advantages**	**Disadvantage**
Increased turbine diameter	Reduced relative velocity, hence reduced erosion	Increased material cost and increased space requirements
Thicker runner blades	Increased time before structural damages has significantly affect of the efficiency	Decreased efficiency and increased risk of of vibrations caused by von Karman vortices
Fewer runner blades	Improved access to the flow channel for coating purposes	May result in reduced cavitation performance
Coating on exposed parts	Increased abrasion resistance of the surface	May increase surface roughness, which may reduce the efficiency. Increased production cost

Table 3.1: Measures to decrease erosion [8]

All measures will increase the cost of the power plant and therefore has to be weighed against the total gain. The coating part has been a challenge as it required a certain amount of space to spray the coating on. Turbines are usually assembled

before coating is applied due to welding may affect the coating. This mkaes it hard to apply coating on turbines smaller than a certain size. Dynavec has come with a solution where the turbine is assembled with bolts in stead of welding and still ensure top performance [19]. This allows for even small turbines to be coated.

4 Francis Turbine Design

This chapter will present the theory basis for the new features included in Khoj and specific theory which is discussed later. A short version of the basic theory behind Khoj can be in Appendix A adapted from Gjøsæter's master thesis [4].

4.1 Blade Thickness

After the number of blades are determined, the blade thickness is chosen. For calculations, the blade thickness has been guessed from the last design. Further, the thickness distribution can also be changed.

The blade thickness has to be large enough to withstand the hydraulic forces the blade is exposed to. The hydraulic forces are the static pressure between pressure and suction side of the blade and the dynamic pressure pulsation, where the static force is the greater one.

Due to the complexity of the runner geometry, a simplified stress analysis has been performed to estimate the minimum thickness required. The blade has been modelled as a straight beem between hub and shroud where the hub is considered to be rigid, while the shroud is assumed to have free-traction in accordance with Saeed (2010) [20]. The hub is then flexible in torsion with respect to the hub and the blade can modelled as a beam clamped at hub and guided at the shroud as shown in Figure 4.9.

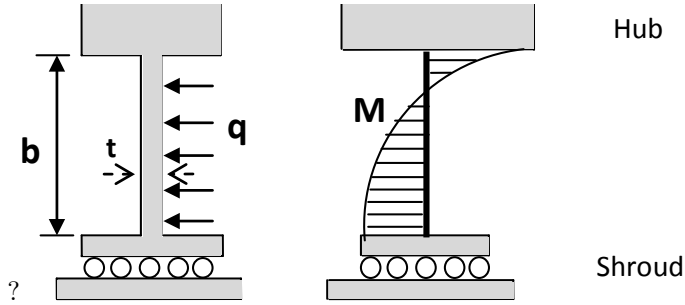

Figure 4.9: Load model of the blade between hub and shroud [4]

Assuming equally distributed load, $q = \Delta r \Delta p$, the bending moment, M, is given by Equation 4.4 [21].

$$M = q\frac{b^2}{3}[Nm] \tag{4.4}$$

The maximum bending stress, σ_{max}, is

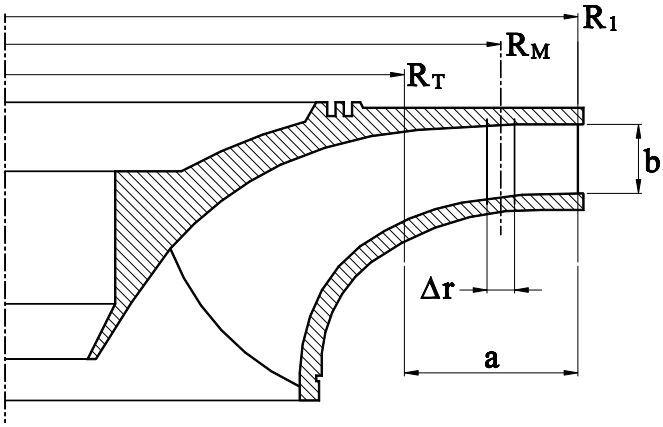

Figure 4.10: Definition of a, b, Δr and R_M [4]

$$\sigma_{max} = \frac{M}{I}\frac{t}{2}[Pa] \tag{4.5}$$

The moment of inertia, I, is given by Equation 4.6, where t is the blade thickness.

$$I = \frac{\Delta r t^3}{12}[m^4] \tag{4.6}$$

The minimum blade thickness at the inlet is found by rearranging Equation 4.4 - 4.6

$$t_{min} = \sqrt{\frac{2b^2\Delta p}{\sigma_{max}}}[m] \tag{4.7}$$

The pressure difference is calculated from torque on the runner. Assuming the entire torque is transferred from the flow to the blade, the imaginary length a is defined as in Figure 4.10 [22].

$$M_{runner} = Z_r a b R_M \Delta p = \frac{P}{\omega}[Nm] \tag{4.8}$$

$$\Delta p = \frac{P}{Z_r a b R_M \omega}[Pa] \tag{4.9}$$

Simulations for Francis turbines with heads of 51 m, 68 m and 79 m indicates static stresses from 95-125 MPa at leading edge and 75-155 MPa on trailing edge [23]. Xiao claims a linear realtionship between power and static stresses at higher heads. The dynamic stresses had a very high amplitude of 15 MPa. This gave a maximum

stress of 196 MPa, with about 1/4 of the ultimate failure strenght of the material used[23]. Saeed has also done similar stress models indicating a maximum stress of 123.5 MPa [20]. In both cases the simulations are performed for lower head turbines than La Higuera, however the highest stress values are from loads greater then found in La Higuera.

Bjørndal et. al. [24] have performed stress measurements in both a high head runner and a low head runner. The peak-to-peak stress variations in the low head runner had a maximum value of 229 MPa. The high head measurements are only presented as relative but he states that high head Francis turbines are not subject to the same increased stresses at low load. At overload the mean tensil stress and dynamic stress amplitude will have negative impact on the runner lifetime due to fatigue.

A comparison between measurements and FEM-analysis of an X-blade Francis turbine indicates good agreement between simulations and measurements. The maximum stresses found for by strain gauge measurements was approximately 65 MPa, while the simulations indicated a maximum stress of 62 MPa [18].

Based on the presented results, the maximum bending stress used for minimum blade thickness calculations are chosen to be 100 MPa. This should be a conservative estimate for the stresses in the runner.

4.2 Blade leaning

One of the most important parameters to pressure balance the runner blade is blade leaning [25]. The blade leaning angle is given as the angle that is normal to the flow direction, meaning; by tilting the vertical inlet you introduce leaning to the blade. It can also be expressed as an angular displacement of each streamline at the inlet. By leaning the blade, the pressure distribution from hub to shroud can be adjusted, hence low pressure zones at hub or shroud can be removed and thereby reduce cross flow on the blade.

Figure 4.11 shows the old Tokke turbine designed without blade leaning. The leading edge will then be vertical to the rotational direction. Figure 4.12a shows traditional blade leaning where the leading edge at shroud has been moved in the opposite direction of rotation. The X-blade design, illustrated in Figure 4.12b, has been used more in the later years.

The pictures in Figure 4.12 are both from Cahua hydropower plant, where the traditional balde leaning was replaced with a X-blade shaped turbine. Wang [26] states that the X-blade design adapts to a wide water head variation with stable operation and excellent cavitation performance. The shape of the leading edge also has significant influence on the pressure distribution at the blade close to the inlet. Especially the curve close to the shroud is important to prevent leading edge cavitation [6].

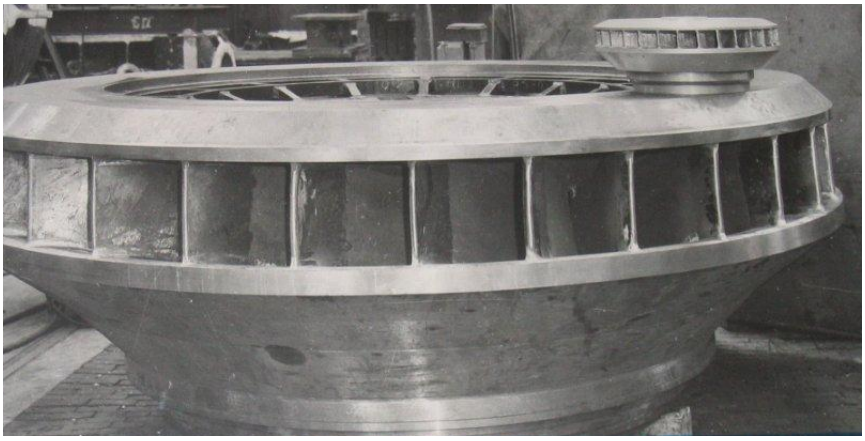

Figure 4.11: Tokke turbine without blade leaning [6]

(a) Traditional design (b) X-blade design

Figure 4.12: Different blade leaning at Cahua hydropower plant [6]

5 Design Procedure

5.1 New features of the program

This section will shortly describe the changes and the development done with Khoj during my thesis. A description of the old version of Khoj can be found in Gjøsæters master thesis [4]. Screenshots from the tabs with major changes can be foun in Appendix C.

5.1.1 Visual changes

The most significant change is the removal of the update buttons. The update function has been implemented in the tab buttons. This has made the program more intuitive and faster, as the next tab is not updated before the user choses it. This also allows the user to skip tabs as the update functions for all previous tabs will run if not done already.

Of practical reasons the program will store the last used values automatically so the next time the program is opened, the last used values will be displayed as initial values.

5.1.2 Main dimensions

The main dimensions tab has got some small changes in variables which can be chosen due to which variables are known for La Higuera. The acceleration is removed and inlet height, B_1, is introduced.

5.1.3 Leading and trailing edge geometry

A new option to choose the leading edge geometry is introduced. The standard design is based on experience as shown in Figure 5.14 [6].

The trailing edge shape is chosen in order to minimize the amplitude of von Karman vortices. The trailing edge is grinded at the suction side of practical reasons due to the grinding is done after the assembly of the turbine. Currently, the trailing edge cannot be changed, but if production methods allow it, the trailing edge shape will be introduced as an active element in Khoj.

The distance noted as R and 3R in red in Figure 5.14, can be specified to generate a different leading edge shape.

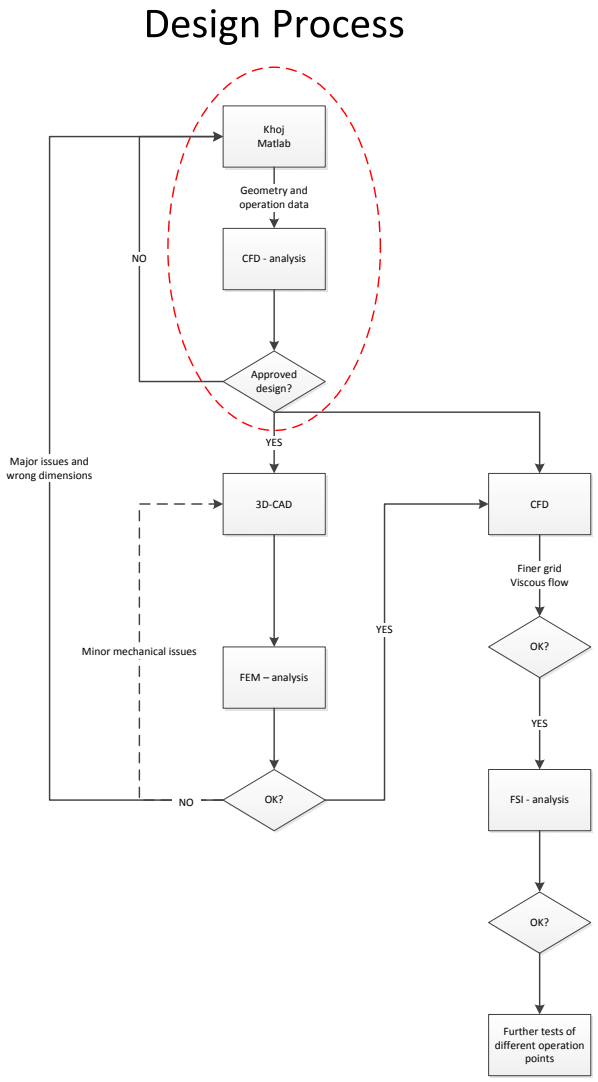

Figure 5.13: Current design procedure. The red ring indicates the working area of this thesis

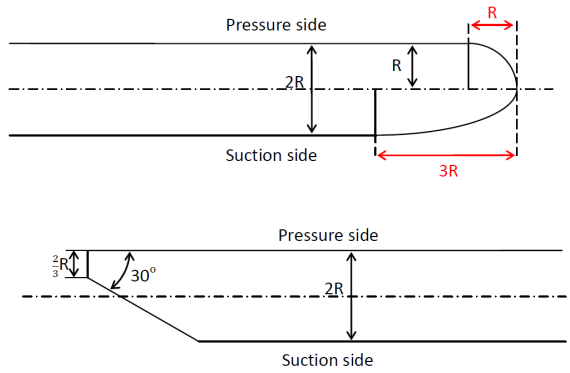

Figure 5.14: Shape of leading and trailing edge [4]

5.1.4 Blade leaning

Blade leaning has been included in the design software to make the user able to pressure balance the blade. There are two options for the blade leaning in the program. For both option the rotational speed remains constant, hence the peripheral velocity U is constant. There also assumed that the blade leaning will not affect the volume flow, hence the absolute velocity in meridional direction C_m is constant.

Figure 5.15 and 5.16 shows the two different options of blade leaning. Both figures illustrates blade leaning of hub in the rotational direction of the runner. Leaning in the rotational direction will increase the pressure on suction side close to hub and reduce the total pressure on the pressure side. This would be correct to do if there was a low pressure zone around hub on the suction side. CFD analysis has to be used to obtain pressure distribution with blade leaning.

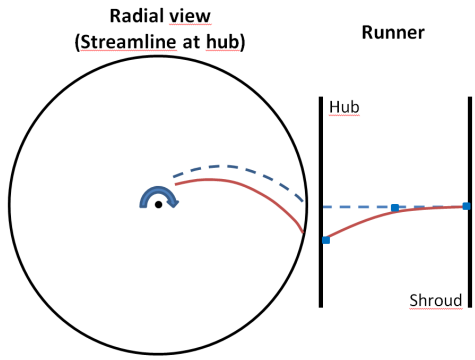

Figure 5.15: Blade with blade leaning option 1

Option 1: In this option blade leaning is introduced to the whole blade from inlet to outlet. This is simply done by rotating each streamline around the rotation axes of the turbine in accordance with the desired blade leaning. This option does not change the streamlines, inlet, outlet angle or C_u, hence, the velocity diagram remains unchanged. The length of the blade will also remain unaltered.

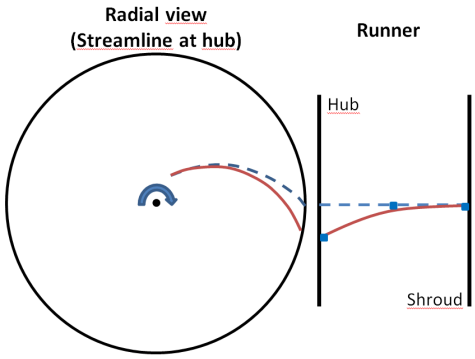

Figure 5.16: Blade with blade leaning option 2

Option 2: However, simulations indicated that there was a need for an option to keep the outlet geometry but still introduce leaning to the inlet. To achieve this, the two last points on each streamline were locked, while the rest of the streamline was rotated. The blade leaning figure was used to determine the degrees the inlet point on each streamline should be shifted. By using linear interpolation and keeping the distance from the rotation centre of the turbine constant for each point, a smooth blade leaning was obtained. By doing this, the outlet velocity diagram remains constant, but the inlet velocity diagram is changed.

Since only parts of the streamline is rotated, the inlet angle β_1 is changed, thereby the relative velocity w and the C_u-component. Hence, the energy distribution, $U \cdot C_u$, is altered because the blade length is altered. Introducing blade leaning in the way shown in the figure will increase β_1. As U_1 and C_m are constant, the magnitude of w_1 is increased and C_{u1} is decreased. Since the trailing edge remains fixed, the velocity diagram for the trailing edge will remain constant.

5.1.5 Guide vanes

A new guide vane tab has been introduced. This tab includes the guide vane, stay vane and spiral casing options. A complete cross-section of the turbine is plotted. For the guide vanes the possibility to choose number of guide vanes, Z_{gv}, the guide vane axis location, D_0, and the overlap factor, k_{ol}. In addition there is introduced an option to import different Naca-profiles as guide vane.

For the stay vanes, the designer has to choose number of stay vanes, Z_{sv}, and the stay vane thickness, t_{sv}. In addition the maximum stay vane stress is presented

as variable. The calculations is done in accordance with chapter 4.7 in Gjøsæters master thesis [4].

5.1.6 Blade thickness

The blade thickness tab has been further developed. The user has the possibility to decide the blade thickness through deciding leading edge and trailing edge thickness. In addition is there an interface for changing the thickness distribution. The minimum thickness according to calculations shown in Chapter 4.1 is displayed as a reference.

6 CFD Theory

CFD is a recognized tool for analysis of hydraulic machinery like Francis turbines. In this thesis, all simulations are accomplished with three-dimensional Navier Stokes solver Ansys CFX 13.0 to verify results from the design software. Ansys CFX was chosen because of in-house experience and previous work of similar problems. Further background information about general CFD-theory can be found in Appendix B.

6.1 Grid properties

A good grid is essential to achieve credible results. The choice of properties will affect the accuracy and convergence of the solution. The governing equations for the physics in fluid domain are based on the principles of Newtons 2nd law, mass and energy conservation (further described in Appendix B). Measures of mesh orthoganality, expansion and aspect ratio are generally used as significant measures for mesh quality. The limitations included in the solver was used as reference. It is important to realize that the measures are intimately related to the solver used and values heavily depend on the discretization method.

To analyse the flow in the domain, the equations is discretized and solved for each node. The Finite Volume Method (FVM) is used in Ansys CFX to to make a set of algebraic equations.

6.2 Mesh Generation

The Automatic Topology and Meshing (ATM optimized) mesh feature was new in the Ansys TurboGrid Release 13.0. Ansys claims this feature generates a high quality mesh with minimal effort [27]. Mesh generation is fast and there has been few issues with negative volumes which were the biggest problem for traditional mesh generation.

Based on experience from Gjøsæter [4] the ATM optimized feature has been used without the 'cut-off and squared' option. For the leading and trailing edge shape, surface type have been chosen to be ruled in accordance with Gjøsæter. This improved the shape of trailing and leading edge and gave no problems with negative volumes.

6.3 Turbulence Modelling

Several turbulence models are available in Ansys CFX. However, not all of them are suitable for fluids in rotating systems or flows dominated by boundary layer behaviour.

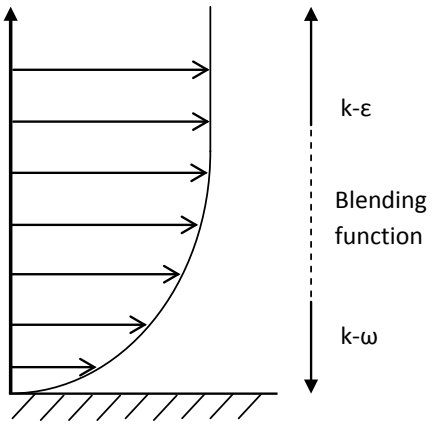

Figure 6.17: SST model [4]

The k-ϵ model is considered as the industry standard dueits stability and numerical robustness. The model is valid for the free stream area, but has its limitations in boundary layer separation, flows over curved a surface and rotating fluids. The achieve accurate results in the viscous sublayer, the k-ω model is used. The k-ω model is robust and provides accurate results in the viscous sublayer. However, it is more computational expensive than the k-ϵ and is very sensitive in the free stream region calculations.

To achieve a turbulence model which could handle the whole near wall region, the Shear-Stress-Transport model (SST) was proposed by Menter [28]. This model uses an automatic near wall function which uses the k-ω model close to the wall and gradually blens into the k-ϵ model in the free stream area as illustrated in Figure 6.17

The mesh resolution is defined by y^+ values, which is a non-dimensional parameter describing the distance from the wall to the nearest node (Equation 6.10).

$$y^+ = \frac{\rho \Delta y u_\tau}{\mu} \tag{6.10}$$

Here, $u_\tau = \frac{\tau_w}{\rho}^{1/2}$ is the friction velocity, Δy is the distance from the wall to the first mesh node and τ_w is the wall shear stress.

Theoretically , a mesh resolution of $y^+ < 2$ [29] is required for the SST model to accurately solve the viscous sublayer. However, such a low y^+ value is hard to obtain for a Francis turbine runner blade. To reduce computational cost, wall functions can used to approximate the near-wall flow. The wall function method assume a logarithmic velocity profile to approach the no-slip condition at the wall as shown in Figure 6.18. The method allows for a much coarser mesh, yielding lower runtime and computer-memory requirements.

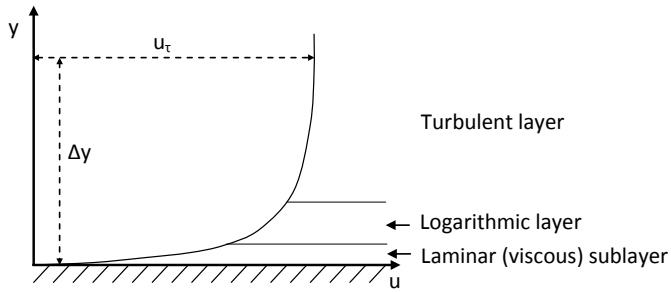

Figure 6.18: Wall function. Adapted from [7]

Solving by using wall functions gives sufficiently accurate results according to several sources. For a Coutte flow, Menter [30] found that the computed shear stress varied by less than five percent when changing the mesh resolution from y^+ 0.2 to y^+ 100. To obtain godd results when using wall function, the mesh cannot be made arbitrary fine according to Apsley. A y^+ between 30 and 150 is suggested by Apsley. This is consistent with Gjøsæter [4] who recommends a y^+ value in the range of 20 - 200 for a Francis turbine runner. It is also impossible to have a constant value of y^+ over the entire blade. The y^+ values on the main part of the blade should be within the recommended range as it is here separation will start. The low y^+ at leading and trailing edge can be disregarded [4].

7 Computational Model for Francis Turbine

It is assumed that every runner blade is equal and will be exposed to the same forces. To save computational cost only one runner blade has been used in the computational model. The geometry of the runner blade geometry has been generated by the design software. The mesh generation and definition of boundary conditions is further described in this chapter.

7.1 Mesh generation

All meshes are generated by the ATM optimized feature in Ansys TurboGrid. The boundary layer refinement control parameters are shown in Table 7.2. The methods and values are chosen based on recommandations from Gjøsæter and Eltvik [31, 32].

Proportional refinement:	
Factor ratio	2
Near wall element size specification:	
Method	y^+
Reynolds number	250 000

Table 7.2: Boundary layer refinement control data

The *Factor ratio* controls the expansion ratio of the mesh cells size from the wall. A small factor ratio of 1.25 is recommended [32**?**]. However, it was impossible to make a mesh with these values that was fine enough to meet the y^+ recommendations without exciding the available computer memory. Increasing the factor ratio to 2.0 allowed for a finer mesh in the near wall region, but had negative effect on the mesh quality. Increasing the ratio to much will lead to convergence problems. Simulations with different factor ratio show the same trends for pressure distribution, but the outlet velocities changes.

7.2 Boundary conditions

To simplify the simulations and reduce computational cost, only one runner blade was calculated. In the post-processing the turbine is assembled with all 17 runner blades. The calculating domain with periodic boundary conditions is shown in Figure 7.20. The blade, hub and shroud are modelled as walls. For the viscous simulations, the no-slip condition was chosen. This implies zero velocity at the wall and a boundary layer which have to be calculated. It is preferable to simplify as much as possible to save computational cost, without significant loss in the result quality. By using inviscid simulations the free slip condition is chosen and thereby disregarding the boundary layer. This implies no friction loss which would lead to increased efficiency and increased relative velocities in the near wall region.

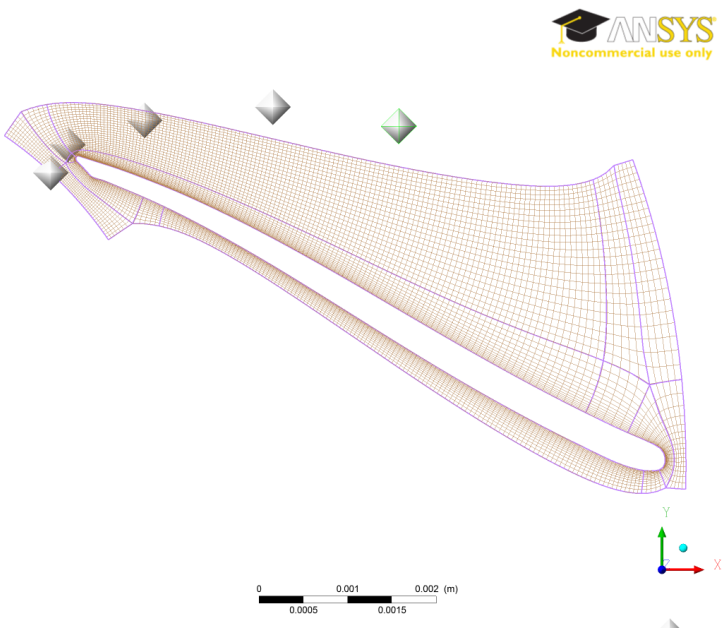

Figure 7.19: TurbiGrid ATM mesh

It is recommended for Francis turbine simulations to specify the mass flow at inlet and total outlet pressure [4, 9]. The flow rate was set 25 m/s^3 and the static pressure at the outlet is equal to one atmosphere. The flow direction at the inlet is specified by cylindrical coordinates. The design software calculates these coordinates. However, this values can only be regarded as initial values as the blade thickness is not taken into account in the calculations. To obtain correct head in the simulations, it is necessary do an iteration for the velocity components. For this, Gjøsæter developed a MATLAB program to run CFX in batch mode [4]. The program runs the simulation and iterates the velocity components until the head is within the specified accuracy of the design head. A head within 0.25% of the design head is acceptable. For the simulations the limit was chosen to be $+/-0.5m$, which is less than 0.15%, was chosen to avoid to large variations of head. The mesh has to be saved as *Combined in one domain, one file* due to the *.pre*-file setup. Saving the mesh in another way is possible, but would require a new *.pre*-file.

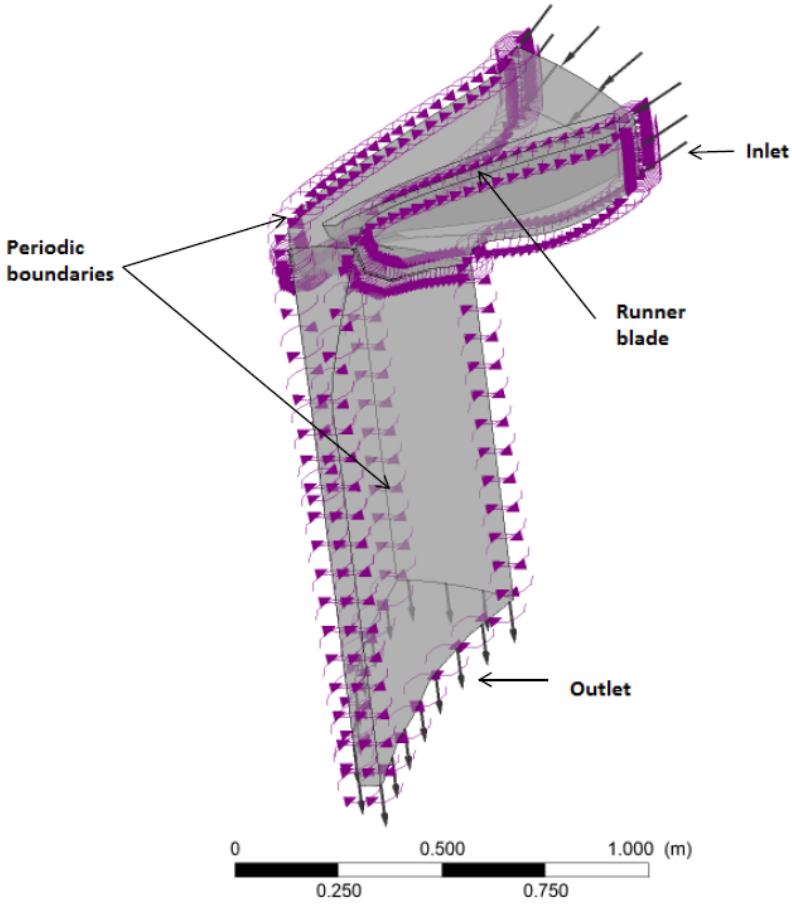

Figure 7.20: Computational domain

8 Reference Design

The turbine data for the previously installed turbine at La Higuera was used as reference design. The known data were used in Khoj to generate a design similar to the previously installed turbine. The objective is to carry out a new hydraulic design with reduced velocity components.

The blade thickness was unknown, so data for this is estimated by using the calculations from Chapter 4.1. The blade thickness chosen to be 36 mm at leading edge and 18 mm at trailing edge. The reference data is listed in Table 8.3

Head	H	353	m
Flow rate	Q	25	m^3/s
Inlet diameter	D_1	2.0	m
Outlet diameter	D_2	1.6	m
Inlet height	B_1	0.226	m
Rotational speed	n	600	rpm
Number of blades	Z_{blades}	17	-
Thickness at leading edge	t_{LE}	25	mm
Thickness at trailing edge	t_{TE}	25	mm
Speed number	Ω	0.4138	-
Submergence requirement	H_s	-9.6165	mWc
Reaction ratio	R	0.5558	-

Table 8.3: Reference Turbine Data

8.1 CFD Analysis

A CFD simulation was carried out to verify the reference design. As the turbine installed in La Higuera was designed for 353 m head, but the location of the intake was moved further up in the hillside after the turbine was designed, the actual head was greater. Head loss measurement shows the actual net head between 370 - 380 m. The reference design was therefore put through simulations on heads at 353 m, 370 m and 380 m to identify any differences in operation at the different heads. Simulations at different head was also used the verify BEP at the reference design from Khoj.

As the net head was changed from what the original turbine was designed for a second reference design was made. This turbine, hereby referenced to as H0, had all the same input parameters as the reference turbine, except the design head was changed from 353 m to 370 m.

Several different meshes was investigated for the reference design at head 353 m. The mesh used for the reference design was chosen due to its y^+-values which was within the range of what is recommended. However, the mesh quality is poor. Different mesh with better quality in accordance with parameters mentioned in

Elements	1
Nodes	1
y^+_{max}	2114
y^+_{min}	4250
y^+_{avg}	59.7

Table 8.4: Reference Turbine Mesh Data

Variable		Design software		CFX		Difference [%]
Head	H	353	m	353.11	m	
Flow rate	Q	25	m^3/s	25.0753	m^3/s	
Efficiency	η	96	%	95.2868	%	0.74
Inlet velocities:						
	U_1	62.8324	m/s	62.8708	m/s	0.06
	C_{m1}	25.3680	m/s	18.3196	m/s	27.78
	C_{u1}	-52.9092	m/s	-53.6428	m/s	1.39
	C_1	58.6764	m/s	56.7239	m/s	3.33
	W_1	27.2398	m/s	21.2694	m/s	21.92
	W_{u1}	9.9232	m/s	9.2282	m/s	7.00
Outlet velocities						
at diameter	D_{ref}	1.2797	m	1.2797	m	
	U_2	40.2030	m/s	40.1919	m/s	0.03
	C_{m2}	16.9795	m/s	15.0016	m/s	11.65
	C_{u2}	0	m/s	-2.7845	m/s	-
	C_2	16.9795	m/s	17.1383	m/s	0.94
	W_2	43.6407	m/s	40.4798	m/s	7.24
	W_{u2}	40.203	m/s	37.4075	m/s	6.95

Table 8.5: Design software data and reference turbine data

Chapter 6, had y^+-values in the magnitude of 10^3. The results were very much alike, but some differences was found in the outlet region as this was where the mesh quality was the poorest. Mesh data for choosen reference design can be found in Table 8.4.

The y^+-values are well out of range for the SST-model to function properly. It was not possibly to achieve the recommended y^+-values with such low *Factor ratio* and without reducing the mesh quality significantly as decribed later.

The CFX results are compared to the design software calculations in Table 8.5. The velocities and angles are more less coincident at the inlet, except for C_{m1} and W_1. At the outlet there are some differences for the meridional velocity, C_{m2}, and the relative velocities. The differences in relative velocities and meridional velocities are most likely linked to the thickness estimation from Khoj. Based on the Matlab values, the meridional velocity is reduced by 33%, while CFD simulation only indicates a deacceleration of 18%.

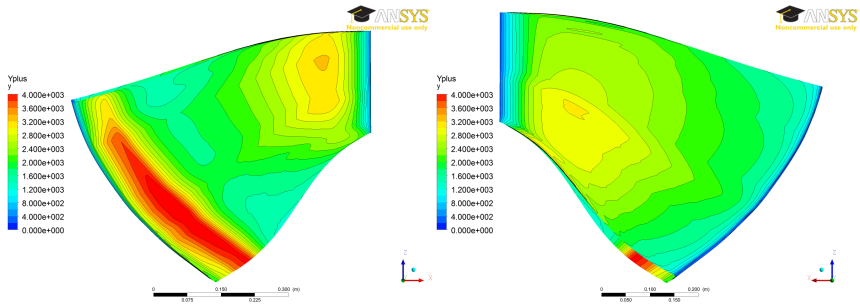

(a) Suction side (b) Pressure side

Figure 8.21: y^+-values on the runner blade formesh with *Factor ratio = 1.1*

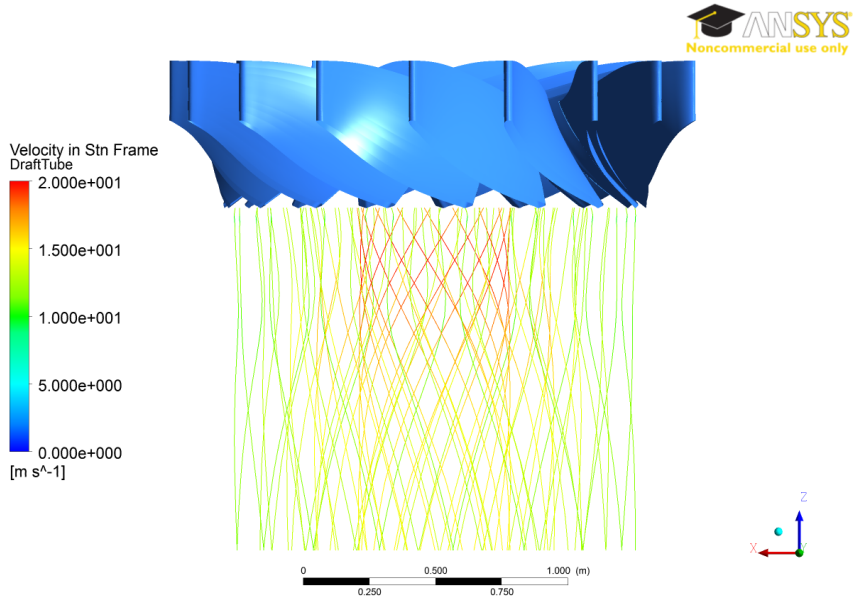

Figure 8.22: Streamlines in draft tube at BEP

No swirl in the flow close to the draft tube wall is prefered, while the swirl in the center is generally considered harmless as long as the C_u velocity is less than 50% of the absolute velocity [6]. The velocities from CFX do not add up exactly to a correct velocity triangle. The hydraulic report from CFX-Post provides a distortion parameter which givesthe ratio between the length of the absolute velocity C and vector sum of C_u and C_m components. A low value of the dissortion parameter is desirable. The distortion parameter has it maximum value at the trailing edge for the reference design at 1.0391, which is acceptable.

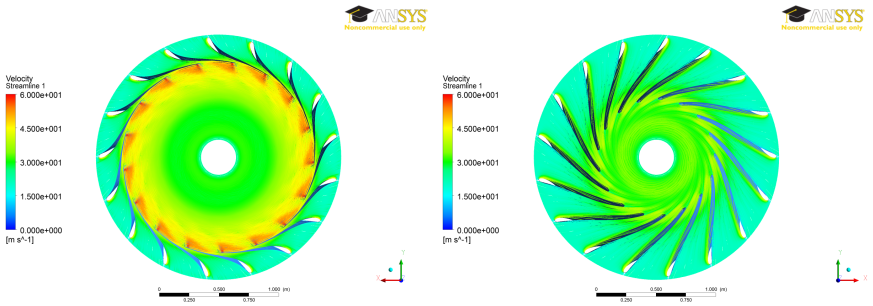

(a) Top view

Figure 8.23: Relative velocity in runner seen from outlet and from top

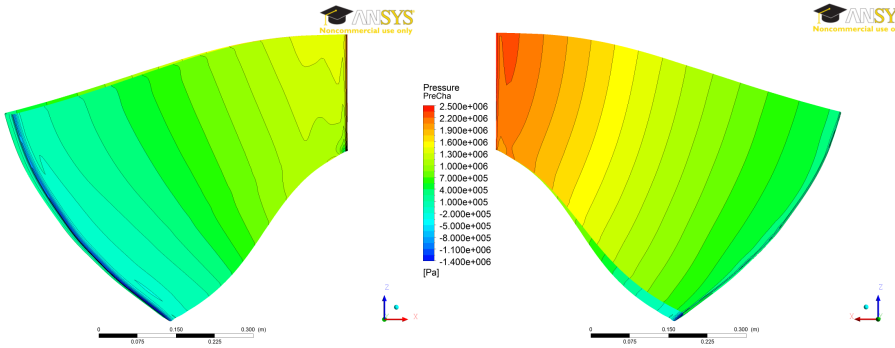

(a) Suction side

(b) Pressure side

Figure 8.24: Static pressure on the blade, reference mesh

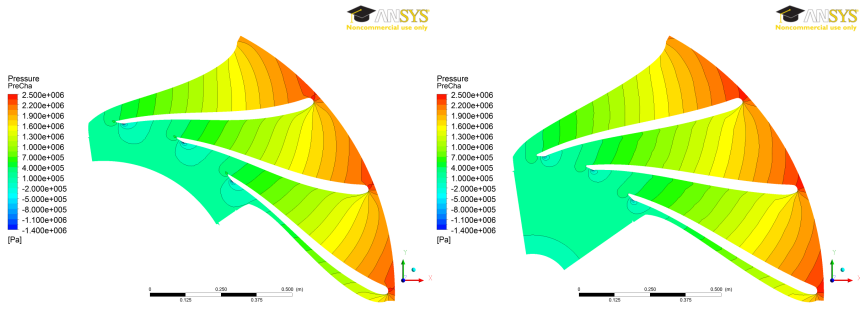

(a) Midway from hub to shroud

(b) hub

Figure 8.25: Pressure distribution between blades

The transition of relative velocity from inlet to outlet is shown in Figure 8.23.

There are no swirl in the blade channels and there is an acceleration in relative velocities shown in Figure 8.23. The design software indicates a deacceleration of the flow through the turbine and the report also indicates a velocity reduction through the runner, but significantly smaller. A deacceleration should be avoided due to easier separation of the flow and backflow.

The pressure distribution on the blade surface is shown in Figure **??**. It is desirable to have a smooth transition from leading to trailing edge with contourlines gradually changing from inlet shape to outlet shape. The pressure distribution on the pressure side of the blade is good except at from close to the leading edge. The pressure is reduced from hun to shroud along the leading edge. At the suction side the uneven pressure distribution becomes more obviuos. Close to the shroud at the leading edge, a low pressure zone has emerged. This low pressure could possibly cause vapor generation, hence cavitation.

Figure 8.25 shows quite decent pressure distribution except from the at trailing edge. Again, there is an undesirable low pressure zone occuring, prone to cause cavitation. The cause of this low pressure zone is not clear. It is suspected that trouble in the modelling of traling edge is some of the cause to this low pressure zone. The blade is imported to Turbogrid as points which defines each streamline. Turbogrid then generates the blade surface by using splines. Unfortunately, this has an undesired effect for sharp edges like around the trailing edge. The use of splines rounds of sharp edges and gives the trailing edge a wavy shape like shown in Figure 8.26

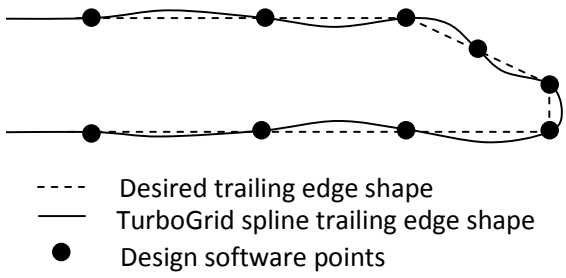

Figure 8.26: Trailing edge shape in Turbogrid, somewhat exaggerated [4]

It is possible this design flaws from turbogrid can be elimated by drawing the turbine in Pro/ENGINEER (Pro/E.) first and exporting it to Turbogrid. This would also remove possible numerical errors from using two different programs to generate a blade for hydraulic and mechanical analysis. However, in the early optimization phase, design flaws like swirl and low efficiency are more critical and a exact blade shape might not be crucial [4].

9 Verification

All CFD simulations should be verified and validated. Verification is the process of determining that a model implementation accurately represents model and the solution correctly. The process quantifies the errors [33]. To minimize mesh errors, mesh independency is a goal. Mesh independency is ensured by refining the mesh until simulations give the same results. A coarser mesh i prefered to use in terms of computer memory and run time requirements.

Validation is the process determining the degree to which the model is an accurate representation of the real world from the perspective of the intended use of the model. [33]. To validate the CFD results, they should be compared to experimental results which would include model testing.

9.1 Multilevel CFD

For optimization studies with CFD is very time consuming if full Navier-Stoke CFD simulation are used. To reduce computational cost and time, multilevel CFD can be used. Multilevel CFD implies that the initial simulations are carried out at a lower accuracy level which will capture trends but not every detail. To use multilevel CFD, the simulations have to be sufficiently accurate to capture the physics correctly.

The simulation time depends on the mesh size and number of equations to solve for each domain. A coarser mesh will have less mesh points, consequently the total number of equations to solve is reduced and thereby the simulation time. By applying invscid calculations the viscous boundary layer no longer need to be solved. Reducing mesh size and using inviscid calculations may significantly reduce the accuracy.

Several different meshes were generated to the same runner geometry to verify the use of multilevel CFD approach. Both viscous and inviscid calculations were used to verify the use of inviscid mesh for the optimization study. The results from different simulations are compared in the following sections.

Table 9.6: Mesh information

Mesh	Nodes	Elements	y^+_{max}	y^+_{min}	y^+_{avg}	Factor ratio
Reference mesh	13183359	1244600	2114	59.7	4250	1.1
Mesh A	588616	558085	331.9	5.57	159.4	2.0

Figure 9.27 shows the reference mesh, while Figure 9.28 shows mesh A. Due to the high y^+-values for the reference mesh, it was chosen to generate a second mesh with lower y^+-values. Mesh data is listed in Table 9.6. There are some minor differences in pressure distribution at the blade. Mesh A indicates lower pressure across the

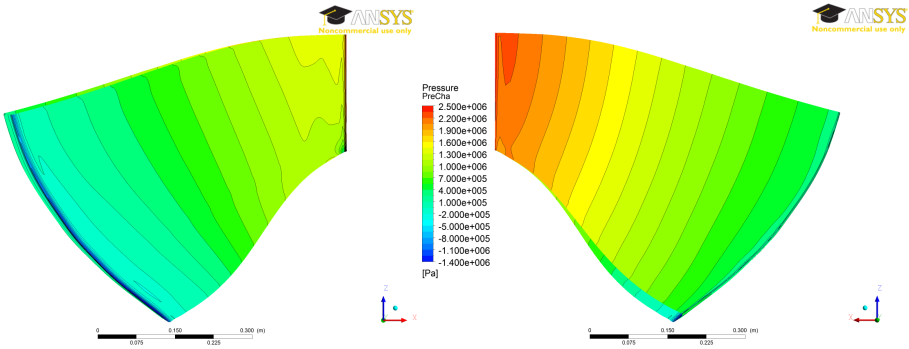

(a) Suction side (b) Pressure side

Figure 9.27: Static pressure on the blade, reference mesh

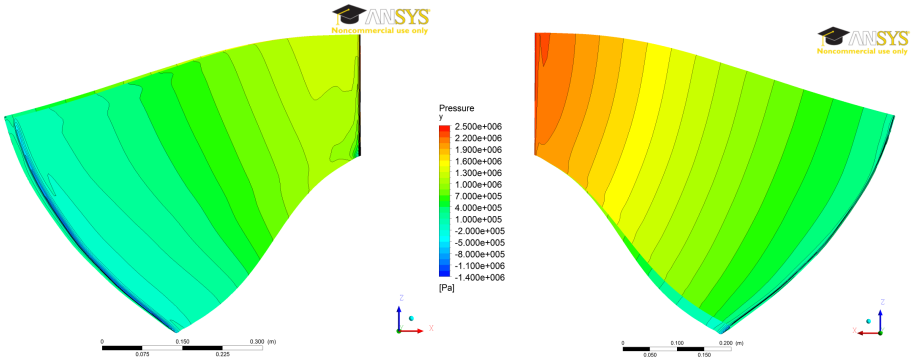

(a) Suction side (b) Pressure side

Figure 9.28: Static pressure on the blade, mesh A

entire blade both at suction side and pressure side, but the tendencies are similar. The low pressure zone at inlet is found at for both meshes and the contour lines have a similar shape.

Comparing the draft tube velocities for both meshes (see Figure 9.29) shows a significant difference in where the maximum velocity is found. The difference in most likely due to the cell quality in the draft tube for mesh A, which is really poor. Therefore, the velocities in the draft tube from simulation with mesh A is disregarded.

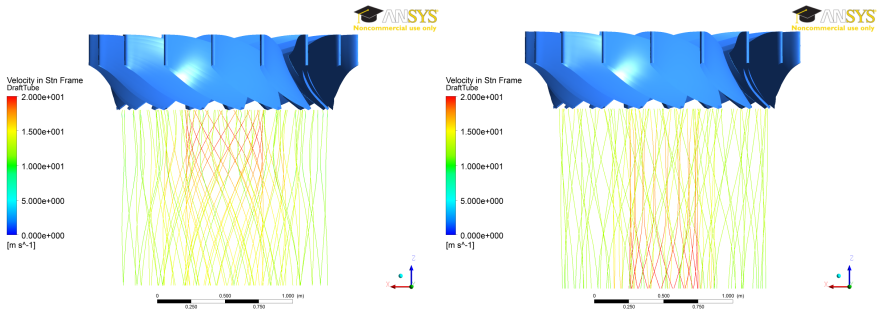

(a) Reference mesh (b) Mesh A

Figure 9.29: Comparison of draft tube velocities

Table 9.7: Mesh information

Mesh	Nodes	Elements	Head (IN-OUT)	Total Efficiency (IN-OUT)
Viscous	130048	118420	352.799	95.26
Inviscid	130048	118420	353.414	98.66

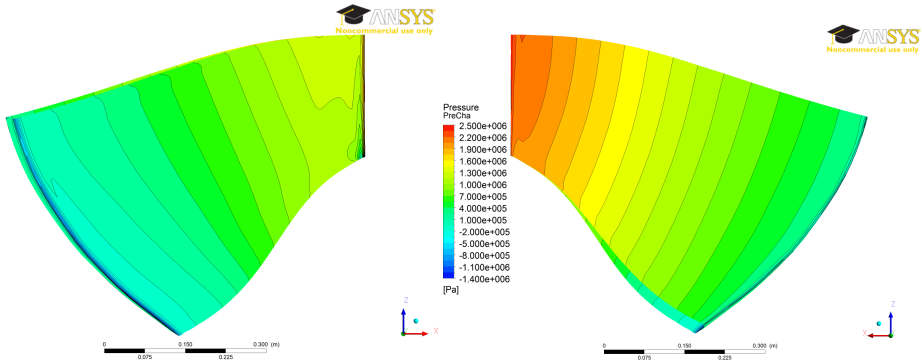

(a) Suction side (b) Pressure side

Figure 9.30: Static pressure on the blade, viscous simulation results

9.2 Coarse mesh

Both coarse mesh simulation gives similar results for pressure distribution along the blade, but the inviscid simulation has a closer resemblance to the fine mesh simulation. However, efficiency has significantly improved for the inviscid simulation which is related to neglection of friction.

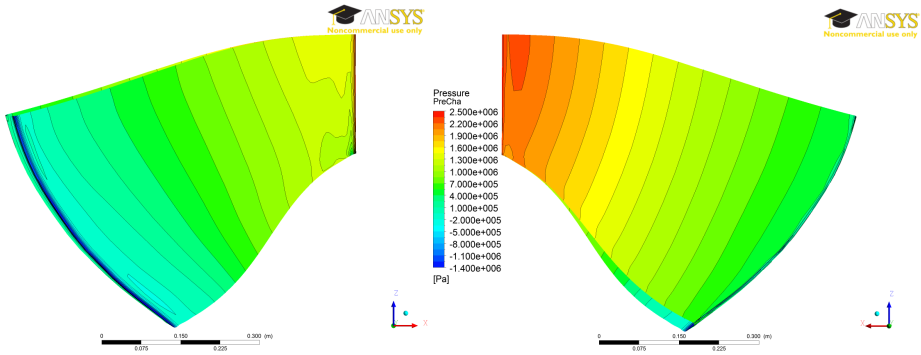

(a) Suction side (b) Pressure side

Figure 9.31: Static pressure on the blade, inviscid simulation results

Summary
Simulation time is strongly dependent on mesh size and calculation method. To properly solve the boundary layer, an y^+-value less than one is required. This would require an extremly fine mesh, which again increases the amount of calculations. Satisfactory simulation results can be achieved if the maximum y^+-value in the critical areas does not surpass 200 [29]. The y^+-values in the simulations presented exceeds that and will need improvment.

However, all simulations show the same trends and it therefore assumed that coarse mesh and invscid simulations are accurate enough for the first stage in the optimization process and also extremly time saving.

10 Results

10.1 La Higuera

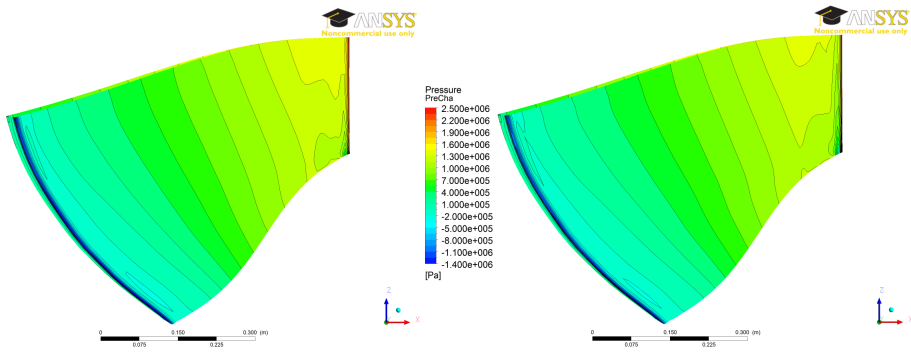

(a) Head 353 m (b) Head 370 m

Figure 10.32: Comparison of the suction side for the reference blade at different heads

Figure 10.32 shows the reference blade at different heads. The low pressure zone has become larger for the increased head, which is likely to cause heavier cavitation.

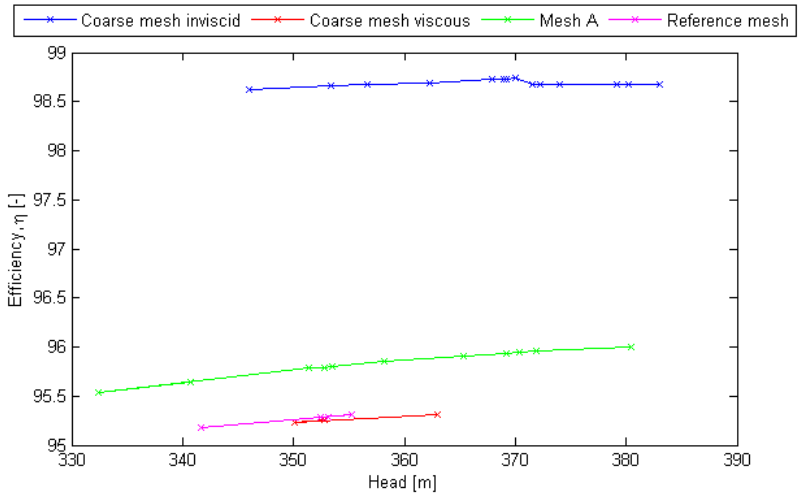

Figure 10.33: Efficiency as a function of head for different mesh

Figure 10.33 shows the efficiency plotted against *Head* for CFD simulation of the reference design with different mesh. It should be noted the difference from viscous simulation to inviscid simulation of approximately 3%. The reference mesh, which has the best mesh quality, has a efficiency of around 95.3%. The viscous simulation with coarse mesh has approximately the same efficiency. Mesh A has the highest efficiency for the viscous simulation. There is a tendency that the efficiency increases with the head.

10.2 Parameter Study

Khoj allows for changing several parameters in order to generate different turbine designs. As different parameters may influence each other, the paramater study has been done by changing one parameter at the time.

As for La Higuera, the turbine diameter and inlet height is constant, and it is therefore not possible to reduce the relative velocities significantly. The main parameter in this study has been efficiency and relative velocity. In addition, the pressure distribution along the blade has been evaluated. Due to the above mentioned restrictions, the submergence requirement will remain fairly constant around -9.6 m.

The erosion factor has been neglected as a parameter, due to the uncertainty. Eltvik [32] claims the erosion factor does not have any correlation with CFD results for two particle fluid flow. CFD results for two particle fluid flows are also strongly mesh dependent [29].

10.3 Design H0

As the net head was changed from what the original turbine was designed for, a new turbine design was made with the design software. This was done to investigate the possibility that only the change in head had caused the cavitation at la Higuera.

Mesh	Head (IN-OUT)	Total Efficiency (IN-OUT)	Power Output
H0	370.410 m	98.85%	89.77 MW
Inviscid reference	353.414 m	98.66%	85.45 MW

Table 10.8: Comparison of H0 design and the reference design, both inviscid simulation and coarse mesh

The H0 design also has the low pressure zone close to leading edge found at the reference design. However, the minimum pressure is not as low as for the reference design tested at a head of 370 m. The small increase in pressure on the pressure side is due to the increased design head. The increased head also gives increased power output.

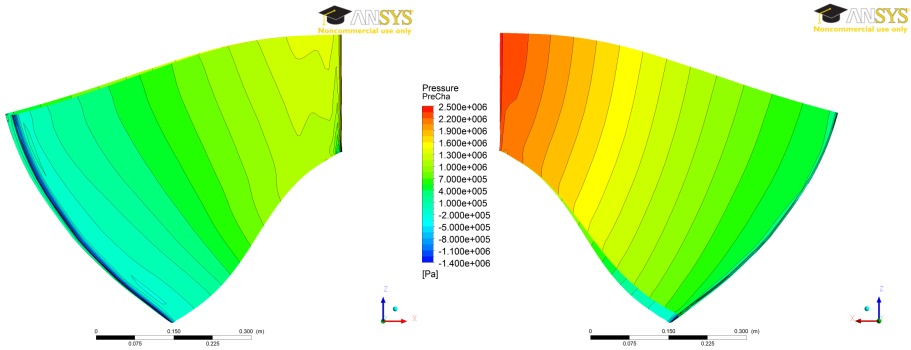

(a) Suction side (b) Pressure side

Figure 10.34: Pressure distribution on the blade for design H0

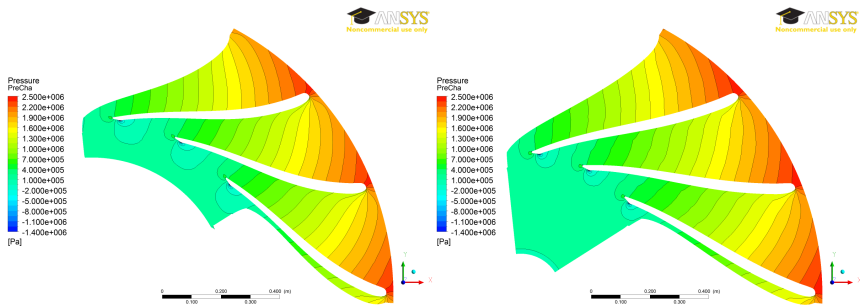

(a) Midway from hub to shroud (b) hub

Figure 10.35: Pressure distribution between blades

Studying the blade to blade pressure distribution at the hub, as shown in Figure 10.35b, the contour lines from the trailing edge and halfway through seem slightly wavy. The pressure lines close to the inlet seem to become more wavy, especially close to the suction side. The pressure distrubition in this region would cause a crossflow towards the suction side. Halfway between hub and shroud as shown in Figure 10.35a, the pressure lines seems to straighten out, but there is still the same tendency close to suction side. However, the pressure distribution midway between hub and shroud seems acceptable.

The draft tube velocities are displayed in Figure 10.36.

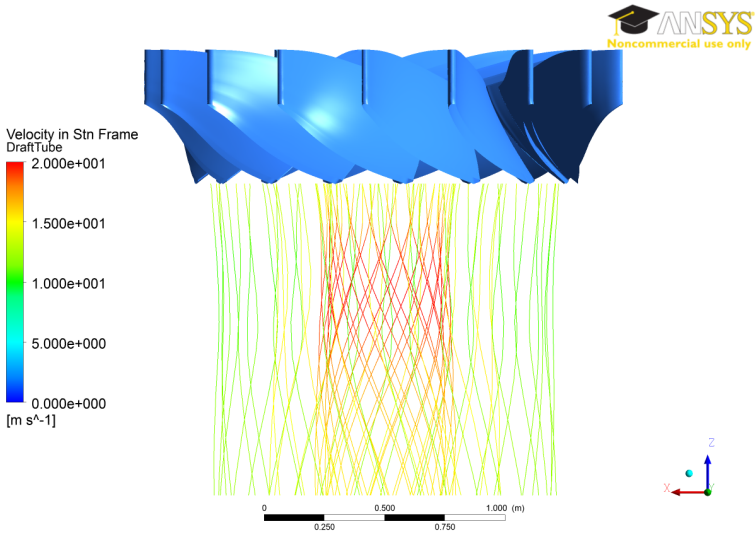

Figure 10.36: Draft tube velocities at BEP for the H0 design

Blade angle distribution	Four different shapes
Blade length	Two different shapes
Blade leaning	Four different shapes

Table 10.9: Parameters for single effects study

10.4 Single parameter studies

10.4.1 Effects of blade leaning

The effects of blade leaning was investigated with several different runner blades. The amount of blade leaning has been defined by how much the hub or shroud line is shifted in degrees from the original position. Simulations was done with both option of blade leaning included in Khoj. To make the results for amount of blade leaning comparable, the shape at the inlet should be similar. A linear blade leaning was chosen to make things simple. It is known that the shape of the leading edge close to the shroud has greatest effect on the blade for pressure balancing [6]

Introducing blade leaning gave positive results compared to reference blade as shown in Figure 10.37. Figure 10.37(a)-(c) illustrates the leading edge shape. The amount of leaning is noted in degrees roted along hub. Figure 10.37(d)-(e) illustrates the corresponding pressure distribution at the suction side of the blade close to the leading edge. In the reference design (Figure 10.37d) there is a large low pressure zone close to the shroud. This is significantly reduced in the two other figures. Figure 10.37e has a small blade leaning resembling toward an X-blade design. With increased blade leaning (5°) as shown in Figure 10.37f, the minimum

pressure is about the same as for 2.5°. However, the shape of the low pressure zone has changed. The smaller blade leaning has a low pressure zone reaching further along the blade, while the greater blade leaning has a low pressure zone reaching longer along the leading edge.

Blade	Head (IN-OUT)	Total Efficiency (IN-OUT)	Power Output
H0	370.410 m	98.85%	89.77 MW
BL1	369.778 m	98.74%	89.52 MW
BL2	369.805 m	98.68%	89.47 MW

Table 10.10: Comparison of H0 design and the reference design, both inviscid simulation and coarse mesh

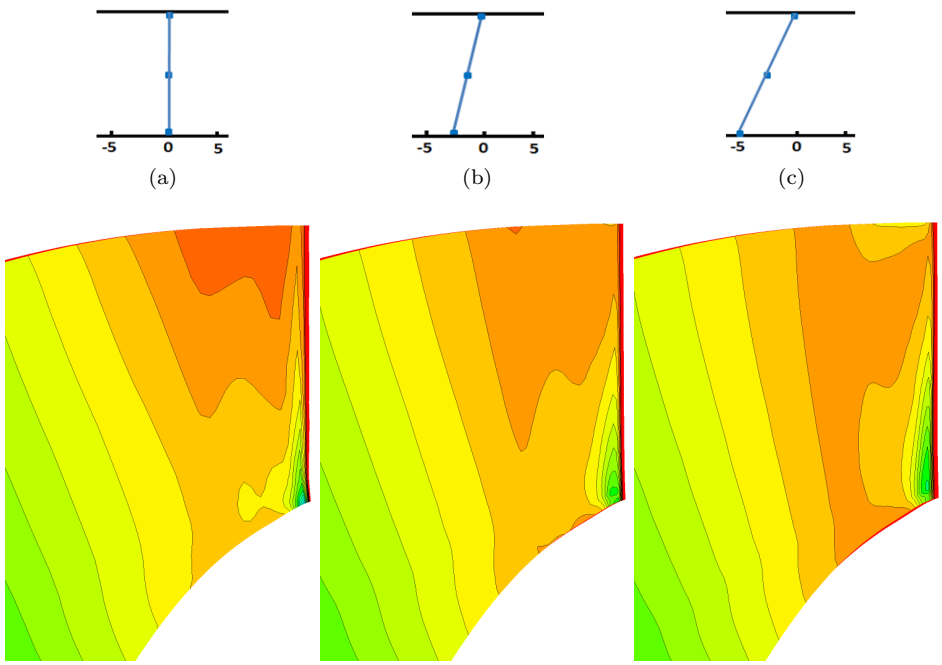

(a) (b) (c)

(d) H0 (e) BL1 (f) BL2

Figure 10.37: Comparisson of different blade leaning

No significant differences could be found between blade leaning by option 1 and 2 for small angles up to 5°. Larger blade leaning was not tested. Introducing blade leaning has been found to have a negative effect on the efficiency.

The pressure distribution in the channel midway between hub and shroud as shown in Figure 10.38a, is acceptable and show the same tendencies as the H0-design. However, at the hub there is indication of low pressure zone forming on the suction side from the leading edge as seen in Figure 10.38b. This is even more evident for

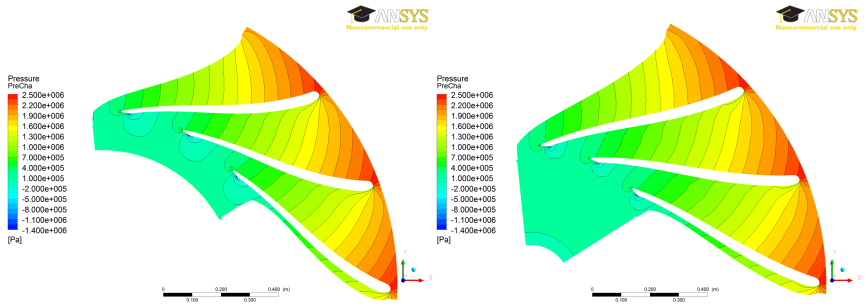

(a) Midway from hub to shroud (b) hub

Figure 10.38: Pressure distribution between blades for BL1

the BL2 design with increased blade leaning. This effect is possible related to effect of linear blade leaning as shown in Figure 10.37(b)-(c). The H0 design indicates the need for pressure balancing close to the shroud. By introducing linear blade leaning, the pressure distribution close to hub is also affected. This is not desirable. An investigation of non-linear blade leaning therefore needs to be carried out to better pressure balance the blade.

10.4.2 Increasing blade length

Blade	Head (IN-OUT)	Total Efficiency (IN-OUT)	Power Output
H0	370.410 m	98.85%	89.77 MW
TE1	369.805 m	98.86%	89.79 MW
TE2	369.827 m	98.99%	89.75 MW

Table 10.11: Comparison of H0 design and the reference design, both inviscid simulation and coarse mesh

This blade is a bit longer simulation indicates a slightly higher efficiency at 98.98%. The pressure distribution again shows the same tendencies. However, it indicates a more severe low pressure zone.

Investigating the pressure distribution between suction side and pressure side, the distribution is similar to the H0-design between the blades. However, the large low pressure zone at the suction side close to trailing edge has almost disappeared at the hub as shown in Figure 10.40b. This migth be related to the length of hub in the radial direction has been increased in this design, while shroud still has the same radial length. This has given greater distance between the points along the hubline, which again will affect the shape of the trailing edge in a positive way and reduce the effect pointed out in Chapter 8.1. Figure 10.40a shows the same tendencies as the H0-design, and the mentioned low pressure zone at trailing edge

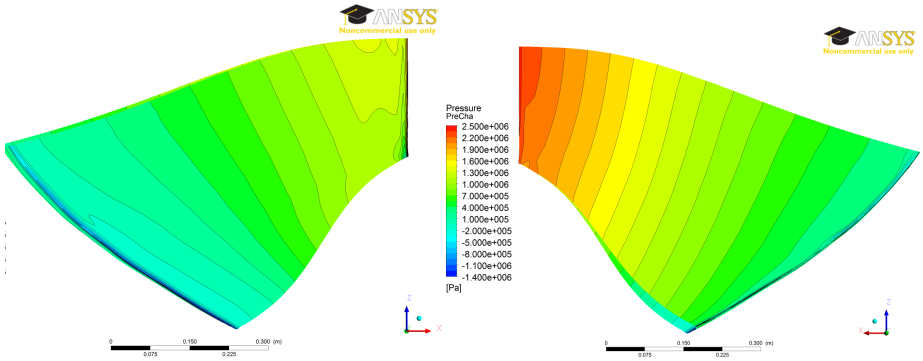

(a) Suction side (b) Pressure side

Figure 10.39: Static pressure on the blade for TE2

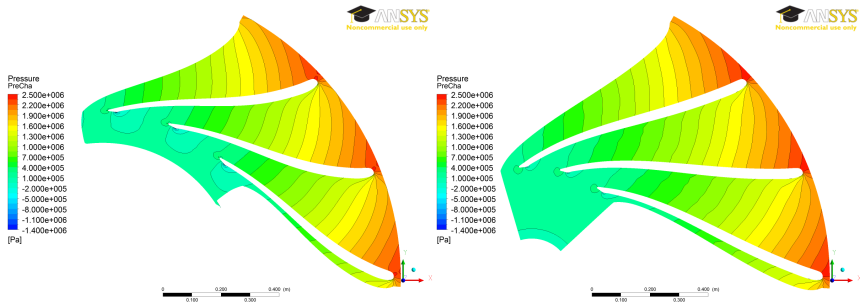

(a) Midway from hub to shroud (b) hub

Figure 10.40: Pressure distribution between blades for TE2

is also clearly visible again.

10.4.3 Effects of changing blade angle distribution

The effect of changing the blade angle distribution has been discussed by Gjøsæter in her master thesis [4]. The Matlab-results are found to resemble Gjøsæter results. The different shapes tested are illustrated in Figure 10.41.

The different shapes causes a change in the energy distribution along the blade. Traditionally a shape similar to Shape 2 is chosen. This shape has an evenly distributed load at the trailing edge [6] and the runner blade is usually thickest at the leading edge and has decreasing thickness towards the trailing edge.

New design philosophy has turned towards Shape 1, as this has lower relative velocities through the runner, but a larger acceleration towards the trailing edge.

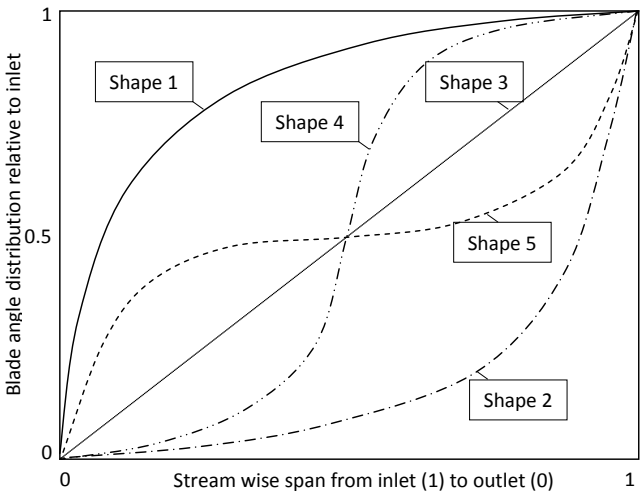

Figure 10.41: Different shapes of the blade angle distribution [4]

This produces an increased load at the trailing edge, which in turn requires a stronger trailing edge.

Blade	Head (IN-OUT)	Total Efficiency (IN-OUT)	Power Output	Erosion Factor
H0 (Shape 3)	370.410 m	98.85%	89.77 MW	1.000
Shape 1	369.813 m	98.90%	89.67 MW	0.771
Shape 2	369.802 m	98.83%	89.60 MW	1.503
Shape 4	369.810 m	98.83%	89.60 MW	1.030
Shape 5	369.798 m	98.84%	89.61 MW	0.839

Table 10.12: Comparison of H0 design and different blade angle distribution

Table 10.12 only show minor differences in efficiency and power output.

Investigating Figure 10.42 does not show any significant differences from the H0-design. The pressure distribution has the same tendencies. Investigation of the low pressure zone close to trailing edge does not show any changes. Some differences can be found in the draft tube velocities for Shape 5. The velocities is somewhat lower than in the H0-design. This could possibly be due to a better β_2-angle and a smaller distortion parameter. The larger core in Figure 10.43 is due to the change in radius for hub.

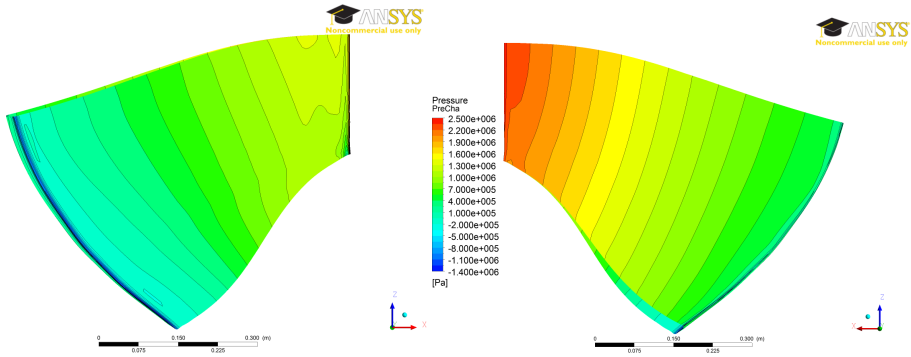

(a) Suction side (b) Pressure side

Figure 10.42: Static pressure on the blade for Shape 1

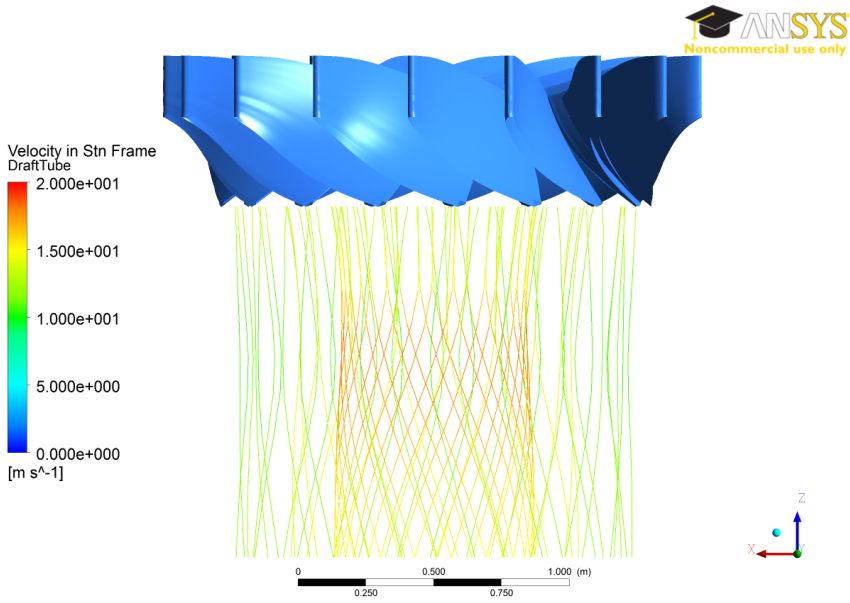

Figure 10.43: Streamlines in draft tube at BEP for Shape 2

11 Discussion

La Higuera Power Plant has been operating under a higher net head than it was designed for. Simulation has indicated a low pressure zone close to the inlet. This low pressure zone becomes more severe with increased head, which would cause heavier cavitation. However, efficiency does not seem to be to much affected by the change in net head. The low pressure zone from the simulations would also be likely to cause cavitation at designed operational head as well.

The unfavourable blade leaning could explain the heavy cavitation experienced in La Higuera.

Blade leaning is an important tool to pressure balance the runner blade. The inviscid CFD simulations with coarse mesh indicate significant changes for the pressure distribution on the blade when blade leaning is introduced. The use of inviscid simulation versus viscous simulation is time saving and requires less computer memory. The differences between inviscid and viscous simulation are so small that inviscid simulation are assumed good enough for the first stage of optimization. The small differences found for the simulation with blade angle distribution might indicate that the inviscid simulation are not accurate enough to investigate the change in energy distribution.

11.1 Blade leaning

The two options for blade leaning were both tested through CFD-analysis. The change in outlet angle and inlet velocities were found to neglectable for blade leaning angles less than 5°. It can be discussed wether both options are necessary for the design software. However, it is likely to see a difference for larger blade leaning. The user should still note the difference between the two options as Option 2 do affect the velocity diagrams, which may cause significant differences for other designs.

The two different blade leaning angles presented in results gave to quite different low pressure zones. It would be easy to assume that increasing blade leaning would only reduce the low pressure zone. However, the low pressure zone of design BL1 is not reduced in BL2, but the shape has changed. For design BL1, the upper half of the blade seem to included in one contour which means quite even pressure. For design BL2, the low pressure zone is stretched toward the hub. This would cause it to affect a larger part of the flow and it could possibly cause a standing wave behind the low pressure zone. The pressure distribution between pressure and suction side at hub was also affected by the linear blade leaning. This suggest a non-linear blade leaning should be investigated. Finding the correct shape could possibly be a very time consuming process of trial by error.

The effect of changing the shape of the leading edge has not been investigated.

11.2 Weaknesses in Khoj

There are two main weaknesses in Khoj; blade thickness and erosion factor. The blade thickness is calculated by a method which should give a conservative estimate. The blade thickness calculations has not yet been verified by mechanical analysis as this is not the scope of this thesis. However, two other methods has been used to calculate the minimum blade thickness. The method based on the empiric formula from Kværner which gave a minimum thickness of 48 mm. The last method applied a simple infinite long plate. This method gave a minimum thickness of 52 mm. Based on experience the method described in Chapter 4.1 was chosen **??**. However, the minimum blade thickness has to verified by FEM analysis.

Error in blade thickness also effects the acceleration parameter in Matlab. CFD simulations show a significantly lower C_m both at leading and trailing edge. The simulations therefore also give a smaller deacceleration through the turbine than Matlab. To achieve acceleration from leading to trailing edge, either inlet area has to be increased or outlet area decreased. La Higuera prefers to keep the current draft tube, which makes it hard to reduce the outlet diameter. The outlet area could possibly be reduced by introducing a cone in the centre of the draft tube, forcing the flow to accelerate to the trailing edge, before deacceleration in the draft tube. A construction like this could possibly cause more problems than gain.

The second weakness is erosion factor. An erosion factor should be included in the design software to give an indication of the erosion rate. Currently the erosion rate i given as

$$E_t = \frac{\sum W_i \cdot A_i}{\sum A_i} [m^3/s^3] \tag{11.11}$$

Dividing by the total area leads to errors, like increasing the curvature of the so the blade area increases, while the relative velocity at inlet and outlet remains constant. The erosion rate will than be reduced, when in reality it is more likely to increase. Dividing by the area is not consistent with any of the erosion models either. It is stated that the erosion rate is proportional to $velocity^3$ which could be used as an indication. However, this is a simplification and will not take into account acceleration. The erosion factor is also limited to compare turbines for the same location as factors such as concentration, material properties and particle properties are ignored.

The erosion factor is included in the part with different blade angle distribution. The erosion factor is significantly lower for Shape 1 and Shape 2 has the definitely worst erosion factor. However, the sudden acceleration close to trailing edge might cause heavy erosion to the trailing edge of the blade of Shape 1. Larger particles will not be able to follow flow exposed to heavy acceleration. The acceleration could possibly lead to a more focused erosion with shorter time before serious damage is inflicted. Therefore, the erosion rate could possibly be much higher than indicated

by the erosion factor. Eltvik [32] has not found any correlation between the erosion factor and erosion simulation in Ansys CFX.

12 Conclusion

Khoj has become more intuitive and easier to use. Some new parameters have been introduced, such as blade leaning. This enables the user to pressure balance the blade which is an important tool to avoid cavitation. Further, an option to include different guidevane shapes has been included.

For La Higuera, this thesis has taken the design process a short way, but there are indications that blade leaning towards an X-blade would reduce the cavitation problem experienced with the previous turbine. CFD simulations indicate a low pressure zone at inlet which could be the cause of heavy leading edge cavitation which increases at of BEP operation. Further the use of inviscid simulation with coarse mesh seem to be accurate enough to pressure balance the blade. Fine mesh simulation need to be performed to confirm this.

Due to the restrictions with regard to changing the guide vanes and generator, it has not been possible to decrease rotational speed or increase diameter. This has limited the possibility to reduce the relative velocities, hence reduce erosion. The best way of reduce erosion will therefore be coating of all wet surfaces. The erosion factor has been neglected because of the great amount of uncertainty associated with it.

13 Further Work

Some of the parameters in Khoj need to be verified, such as the minimum thickness. The estimation of outlet velocities also has it faults. The estimation used give good results in some cases, but a more accurate estimate should be used. However, this may make Khoj significantly slower as every calculation done earlier has do be done again as a change in geometry possibly could change β_2 and C_m.

The erosion factor also has to modified to give a more accurate impression of how the erosion is affected by different changes. Comparison with CFD results and measurements are needed.

Further, there is expected new versions of the program. The Labyrinth tab has to be improved and different labyrinth options should be included. The runner cascade tab will be developed to display a 3D view of the complete turbine with visibility options.

As Jonas Bergmann Paulsen in his project thesis has described how to make a runner blade in Pro/E. it would be interesting to put the design from Khoj straight into Pro/E. or simiiar CAD-tool. A geometry made in a CAD-program may eliminate the problems with spline function at the trailing edge and produce a more correct blade shape.

As La Higuera Power Plant include two turbines, it would be interesting to investigate the possiblity to remove the guidevanes in one of the turbines and only use it as base load. The other turbine could than be used to cover the peak load. This could possibly reduce the relative velocities significantly and thereby erosion.

Due to lack of time, there has been done no analysis of the runner with guide vanes and stay vanes. An investigation of changing diameter of the runner and length of guide vanes could be done to investigateto posssibility to reduce the relative velocities in the runner.

References

[1] G. W. Stachowiak and A. W. Batchelor. *Engineering Tribology*. Elsevier Butterworth-Heinemann, Amsterdam Boston, 3rd edition edition, 2005. ISBN 9780750678360 0750678364.

[2] X. Escaler and et.al. Detection of cavitation in hydraulic trubines. *Mechanical Systems and Signal Processing*, 20(4):983–1007, 2006.

[3] P. Kumar and R. P. Saini. Study of cavitation in hydro turbines - a review. *Renewable and Sustainable Energy Reviews*, 14(1):374–383, 2010.

[4] Kristine Gjøsæter. *Hydraulic design of Francis Turbine Exposed to Sediment Erosion*. Master thesis, NTNU, Waterpower laboratory, NTNU, Trondheim, 2011.

[5] Bhola Thapa. *Sand Erosion in Hydraulic Machinery*. PhD thesis, NTNU, Trondheim, 2004.

[6] Prof. Ole Gunnar Dahlhaug. Personal conversations, November 2011.

[7] Ansys CFX release 13.0 CFX-solver modeling guide. Technical report, Ansys, 2010.

[8] IEC hydraulic machines - guide for dealing with abrasive erosion in water (draft). Technical report, International Electrotechnical Commission, 2008.

[9] Sediment erosion in francis turbines. Master thesis, NTNU, Waterpower laboratory, NTNU, Trondheim.

[10] Under the influence - 60 most influential people in the industry. http://www.waterpowermagazine.com/story.asp?storyCode=2054314, 2011. URL `http://www.waterpowermagazine.com/story.asp?storyCode=2054314`.

[11] Arne Kjølle. Hydropower in norway: Mechanical equipment, 2001. URL `http://www.magnu.polymtl.ca/contenu/ressources/docDivers/doc/Turbines101.pdf`.

[12] Luca d'Agostino and Maria Vittoria Salvetti, editors. *Fluid Dynamics Cavitation and Cavitating Turbopumps*, volume 496. CISM, Udine, 2007.

[13] M.K Padhy and R. P. Saini. A review on silt erosion in hydro turbines. *Renewable and Sustainable Energy Reviews*, 12(7):1974–1987, 2008.

[14] Xi-bin Huang and Yin-zhong Yuan. Mechanism and prediction of material abrasion in high-velocity sediment-laden flow. *Journal of Hydrodynamics*, 18(6):760–764, 2006.

[15] V.Y. Karelin and C.G. Duan. *Design of hydraulic machinery working in sand laden water*, volume 2. Imperial College press, London, 1. edition edition, 2002.

[16] Einar Bardal. *Korrosjon og korrosjonsvern*. Tapir Forlag, NTH, Trondheim, 1. edition edition, 1985. ISBN 82-519-0700-4.

[17] G.F Truscott. A litterature survey on abrasive wear in hydraulic machinery. *Wear*, 20(1): 29–50, 1972.

[18] H. Bjørndal, A. P. Reynaud, and A. L. Holo. Mechanical robustness of francis runners, requirements to reduce the risk of cracks in blades. Prague, Czech Republic, September 2011.

[19] O.R. Valmot. Løst en av vannkraftens største utfordringer. http://www.tu.no/energi/article267678.ece, December 2011. URL `http://www.tu.no/energi/article267678.ece`.

[20] R. A. Saeed, A. N. Galybin, and V. Popov. Modelling of flow-induced stresses in a francis turbine runner. *Advances in Engineering Software*, 41(12), 2010.

[21] Fridtjov Irgens. *Formelsamling mekanikk*. Tapir akademiske forlag, Trondheim, 3rd edition edition, 2005. ISBN 82-519-1506-6.

[22] Hermod Brekke. *Pumper & Turbiner*. Vannkraftlaboratoriet NTNU, Trondheim, 2003.

[23] Ruofu Xiao, Zhengwei Wang, and Yongyao Luo. Dynamic stresses in a francis turbine runner based on Fluid-Structure interaction analysis. *Tsinghua Science & Technology*, 13(5):587–592, 2008.

[24] H. Bjørndal, T. Moltubakk, and H. Aunemo. Flow induced stresses in a medium head francis runner. In *The behaviour of hydraulic machinery under steady oscillatory conditions*, Trondheim, June 2011.

[25] Hermod Brekke. State of the art in turbine design, 2001.

[26] Fu-jun Wang and et.al. Experimental investigation of characteristic frequency in unsteady hydraulic behaviour of a large hydraulic turbine. *Journal of Hydrodynamics*, 21(1):12–19, 2009.

[27] Ansys TurboGrid release. release notes. Technical report, Ansys, 2010.

[28] Florian R. Menter. Two-Equation Eddy-Viscosity turbulence models for engineering applications. *AIAA Journal*, 32(8), 1994.

[29] Stud. Tech. Martin Holst. Personal conversations, November 2011.

[30] Florian R. Menter. Review of the Shear-Stress transport turbulence model experience from industrial perspective. *International Journal of Computational Fluid Dynamics*, 23(4), 2009.

[31] Research assistent Kristine Gjøsæter. Personal conversations, November 2011.

[32] PhD. Mette Eltvik. Personal conversations, December 2011.

[33] H.K. Versteeg and W. Malalasekera. *An Introduction to Computational Fluid Dynamics*. Pearson Education Limited, Edinburgh, 2. edition edition, 2007.

A Background information on the design sofware

This chapter presents the theory behind the design software Khoj. The design method is to a large extent based on the method most commonly used at the Waterpower Laboratory, but with some exceptions where other methods are found more suited and provided better results [4].

4 Francis Turbine Design

This chapter presents the theory basis for the design software. The design method is to a large extent based on the method most commonly used at the Waterpower Laboratory, but with some exceptions where other methods are found more suited and with more correct results. Most of this chapter is taken from the authors project thesis [18]. The chapter is included to give an assembled presentation of the design software theory basis. In addition, the software has been extended and revised with minor and major changes, hence new theory is prevailing. Sections 4.2, 4.3 and 4.5 contain new or revised paragraphs.

Alternative design procedures are hard to retrieve from turbine producers, as this is considered as classified information. However, designing a pump impeller is similar to designing a Francis turbine, and pump impeller design can be reviewed in Stepanoff [19] and Lazarkiewicz [20].

4.1 Introduction

A traditional Francis turbine consists of a runner, a set of guide vanes, a set of stay vanes and a spiral casing, as shown in figure 4.1. The design process starts with the runner and moves outwards, ending with the spiral casing.

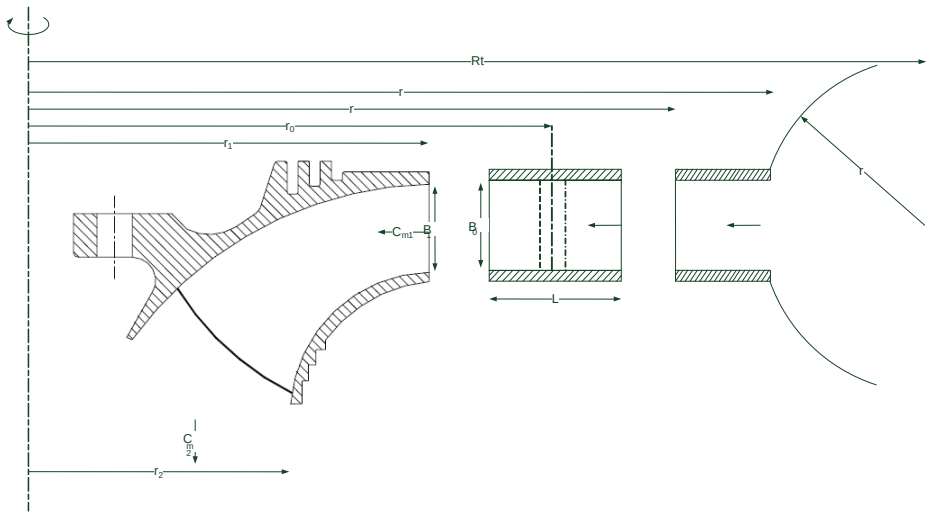

Figure 4.1: Axial view of a turbine [3]

4.2 Main Dimensions

Designing a Francis runner starts with calculating the main dimensions. These are based on hydraulic parameters like head H_e and discharge Q, which are determined by the topography and hydrology of the power plant site. Traditionally, velocity triangles at the inlet and outlet of the runner, as shown in figure 4.2, are used in the design process.

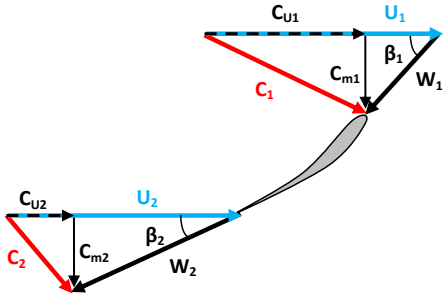

Figure 4.2: Velocity triangles

Dimensions at runner outlet

As a first attempt, the outlet angle β_2 and peripheral speed U_2 can be chosen based on empirical data. Brekke [21] states that for traditional Francis runners these values are usually found in the intervals

$$15^\circ < \beta_2 < 22^\circ \tag{4.1}$$

$$35 \quad m/s < U_2 < 42 \quad m/s \tag{4.2}$$

where β_2 takes lower values for higher heads and U_2 takes higher values for higher heads. The listed intervals should not be considered fixed limits, especially when designing turbines that will be operated in silty water. Measurements at Jhimruk show that the existing runners have a lower outlet peripheral speed than what traditionally is suggested.

At best efficiency point (BEP) no swirl in the draft tube has to be assumed. Hence the peripheral component of the absolute velocity, C_{u2}, equals zero, and the meridian component of the absolute velocity can be found from the velocity triangles.

$$C_{m2} = U_2 \cdot \tan \beta_2 \qquad [m/s] \tag{4.3}$$

With these parameters the outlet diameter D_2 can be calculated from continuity.

$$D_2 = \sqrt{\frac{4Q}{\pi \cdot C_{m2}}} \qquad [m] \tag{4.4}$$

However, this is only strictly valid for infinitely thin blades: Due to the thickness of the blades at the trailing edge, the effective outlet area will be smaller. To find a rough estimate of the outlet area, the number of blades and the thickness of the blade at the trailing edge have to be decided or guessed. Because of the outlet blade angle β_2, the lost area must be approximated as the projection of the blade thickness in the outlet plane, as shown in figure 4.3.

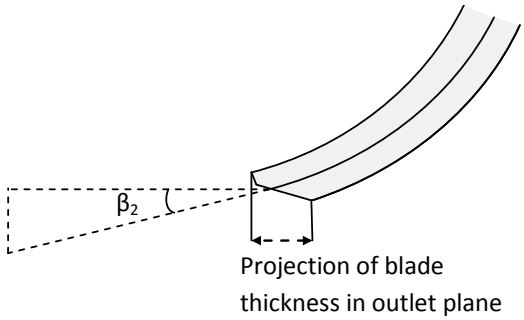

Figure 4.3: Projection of the blade thickness into the outlet plane

Choosing to keep the value of D_2, the C_{m2} value is recalculated taking the lost area into account. However, because β_2 is dependent on C_{m2}, a small iteration loop is necessary to fulfil the no swirl condition.

Knowing D_2, the rotational speed of the turbine can be calculated according to equation 4.5.

$$n = \frac{U_2 \cdot 60}{\pi \cdot D_2} \qquad [rpm] \tag{4.5}$$

The grid frequency in Nepal is 50 Hz. In order to obtain a frequency of 50 Hz, the generator rotor has to pass 50 pole pairs in the stator per second.

$$Z_{poles} = \frac{f_{grid} \cdot 60}{n} \qquad [-] \tag{4.6}$$

The number of pole pairs has to be an integer. To fulfil this requirement, the rotational speed has to be corrected to the corresponding synchronous speed found by rearranging equation 4.6. The designer has to choose whether to round up or down the number of pole pairs. Choosing a higher Z_p yields a larger and slower rotating turbine. According to Verma [22], the sediment erosion damage is less in large machines than in smaller ones. By selecting the speed of rotation one or two steps lower than for turbines operated in clean water, the machine size is increased. Thus the relative flow velocities are reduced with consequently less erosion damage.

Dimensions at runner inlet

When the outlet dimensions are set, the inlet of the runner is to be designed. The designer chooses the inlet peripheral speed, and with that the inlet diameter as well.

$$D_1 = \frac{U_1 \cdot 60}{n \cdot \pi} \qquad [m] \tag{4.7}$$

It is convenient to use *reduced values* in the design process because the reduced velocities are dimensionless. The reduced values are denoted by an underscore.

$$\underline{U}_1 = \frac{U_1}{\sqrt{2 \cdot g \cdot H_e}} \qquad [-] \tag{4.8}$$

The Euler equation is commonly used for turbine design, and is defined as shown in equation 4.9.

$$\eta_h = \frac{C_{u1} \cdot U_1 - C_{u2} \cdot U_2}{g \cdot H_e} \qquad [-] \tag{4.9}$$

By introducing reduced values and including the assumption of no swirl flow in the draft tube at BEP, the Euler turbine equation reduces to:

$$\eta_h = 2 \cdot \underline{U}_1 \cdot \underline{C}_{u1} \qquad [-] \tag{4.10}$$

It is common to assume a hydraulic efficiency η_h of 96 % for the runner.

In order to avoid back flow in the runner, an acceleration of the flow through the runner is desirable. Generally, ten percent is chosen, but this is up to the designer.

$$C_{m2} = (1 + \frac{Acc}{100}) \cdot C_{m1} \qquad [m/s] \tag{4.11}$$

The inlet area can now be found according to continuity.

$$C_{m1} \cdot A_1 = C_{m2} \cdot A_2 \tag{4.12}$$

As was done at the outlet, the runner blade thickness has to be accounted for also at the inlet. The inlet diameter is fixed due to equation 4.7, so the blade thickness will only affect the runner inlet height B_1, as shown in equation 4.13. By combining equations 4.11 and 4.12, the inlet height can be calculated as

$$B_1 = \frac{A_1}{\pi \cdot D_1 - Z_{blades} \cdot \frac{t_{LE}}{\sin \beta_1}} \qquad [m] \tag{4.13}$$

where β_1 is found from equation 4.14.

$$\tan \beta_1 = \frac{C_{m1}}{U_1 - C_{u1}} \qquad [-] \tag{4.14}$$

Submerging the turbine

If the water pressure in the runner is lower than the vapor pressure, cavitation may occur. The impact of gas cavities collapsing close to the wall surface causes cavitation erosion. In order to avoid the water pressure to drop below the vapor pressure, the turbine can be submerged. The required level of submergence, expressed as Net Positive Suction Head (NPSH) depends on the main dimensions and the speed number Ω of the runner. The speed number is a non-dimensional expression for rotational speed at a given head at BEP.

$$\Omega = \underline{\omega} \cdot \sqrt{\underline{^{*}Q}} \qquad [-] \tag{4.15}$$

Knowing the speed number, the required NPSH can be calculated as

$$\mathrm{NPSH}_{\mathrm{required}} = a\frac{C_{m2}^2}{2 \cdot g} + b\frac{U_2^2}{2 \cdot g} \qquad [mWc] \tag{4.16}$$

where the parameters a and b are empirical constants, and, according to Brekke [21], dependent on the speed number.

Ω<0.55 gives a=1.12 and b=0.055

Ω>0.55 gives a=1.12 and b=0.1·Ω

NPSH has to fulfil the following requirement to avoid cavitation

$$\mathrm{NPSH}_{\mathrm{required}} < h_{atm} - h_{va} - H_s \qquad [mWc] \tag{4.17}$$

where

h_{atm} - atmospherically pressure, 1 atm = 10.3 mWc

h_{va} - vapor pressure

H_s - submerging of the turbine. A negative value of H_s implies that the turbine is set below tail water level.

Runners are often designed for high velocities to keep the dimensions down. This results in low water pressures and possible cavitation damage. A turbine designed with low velocity components to reduce the sediment erosion is likely to have larger dimensions than a traditional Francis runner, and hence possibly less cavitation problems.

Traditionally, turbines are designed based on head and flow, assuming sediment free water. Experiments have shown that components, which are cavitation free when operated in clean water, cavitates when operated in silty water [23].

The required submergence is calculated based on the vapour pressure of clean water. The viscosity of silty water is higher than for clean water, hence the vaporizing pressure is higher as well. This causes cavitation to occur at higher pressure levels for silty water than for clean water operation [24].

In addition, sediment erosion and cavitation are inducing each other. An already cavitation pitted surface is more prone to sediment impacts, which intensifies the damage. Likewise, a sediment eroded surface has local flow conditions which induce cavitation at an earlier stage than in clean water, and hence accelerates the damage mechanism vastly.

A deeper submergence of the turbine will avoid cavitation erosion, and thus also the 'cavitation - sediment erosion' synergy. The extent of the additional required submergence is dependent on several parameters, including concentration and size of the particles.

4.3 Runner Blades

When the main dimensions of the runner are known, the runner blades can be designed. The design procedure starts by determining the shape of the blade in the axial view, then the radial view is established, and finally the runner blade can be plotted in three dimensions.

Runner axial view

At first a streamline along the shroud or along the hub has to be defined. It is most common to define it along the shroud. Traditionally an elliptical or circular shape is chosen for the streamline.

After the first streamline is defined, the number of streamlines has to be chosen. The distribution of streamlines is determined by the velocity profile at the inlet of the runner, which initially is considered uniform. This gives a uniform distribution of the streamlines between the hub and shroud at the inlet.

Based on the inlet distribution and the definition of the first streamline, the rest of the streamlines can be determined. A point i on streamline $j+1$ is found by drawing a line between the points $(i+1, j)$ and $(i-1, j)$. Then the new point, $(i, j+1)$, is placed on an axis orthogonal to this line going through point (i, j), as shown in figure 4.4.

From figure 4.4 the following expressions can be derived:

$$\alpha_{i,j} = \tan^{-1}\left(\frac{Z_{i-1,j} - Z_{i+1,j}}{R_{i-1,j} - R_{i+1,j}}\right) \qquad [-] \tag{4.18}$$

$$r_{i,j} = \frac{R_{i,j} + R_{i,j+1}}{2} \qquad [m] \tag{4.19}$$

$$A_{i,j} = 2\pi \cdot r_{i,j} \cdot b_{i,j} \qquad [m] \tag{4.20}$$

$$b_{i,j} = \frac{R_{i,j+1} - R_{i,j}}{\sin \alpha_{i,j}} \qquad [m] \tag{4.21}$$

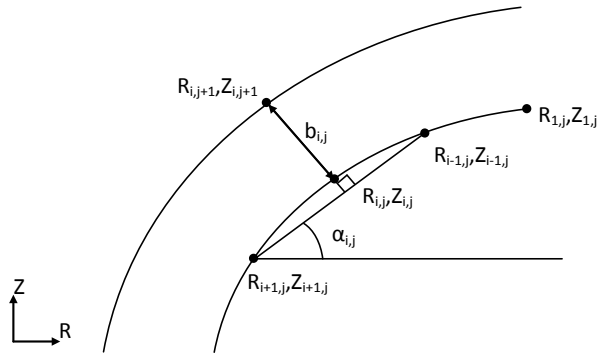

Figure 4.4: Determining a new point on a streamline. Adapted from Eltvik et al. [3]

Combining equation 4.19-4.21 yields:

$$A_{i,j} = 2\pi\left(\frac{R_{i,j+1} + R_{i,j}}{2}\right)\left(\frac{R_{i,j+1} - R_{i,j}}{\sin\alpha_{i,j}}\right) = \frac{\pi}{\sin\alpha_{i,j}}(R_{i,j+1}^2 - R_{i,j}^2) \quad [m^2] \tag{4.22}$$

Expression equation 4.22 can be rearranged to:

$$R_{i,j+1} = \sqrt{R_{i,j}^2 + \frac{A_{i,j}\sin\alpha_{i,j}}{\pi}} \quad [m] \tag{4.23}$$

Finally, the Z coordinate can be found:

$$Z_{i,j+1} = Z_{i,j} - b_{i,j}\cos\alpha_{i,j} \quad [m] \tag{4.24}$$

A common issue when defining the first streamline along the shroud is that the streamlines close to the hub curve upwards at the inlet instead of going in a straight line, bending down towards the outlet. This is an undesirable design feature that must be corrected before proceeding with the design.

Starting with the first streamline along the hub avoids the problem with upward curvature, but it causes other problems, such as lines crossing each other at the inlet, which could result in numerical problems.

Considering these issues, a more general shape of the first streamline would be desirable. Then the problems of upward curvature could be avoided, even when starting from the shroud. An example of a more general curve definition is the Bezier curve.

When the curvature issue has been corrected, the design may need some further adjustments if the runner blades are too close to the centre of the shaft. Removing some of the endpoints on each streamline will solve this problem. If the endpoints

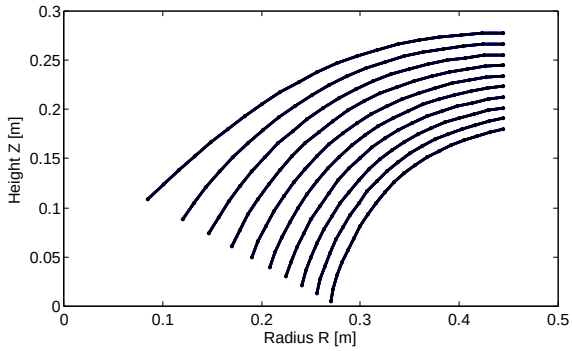

Figure 4.5: Axial view of the runner blade after cutting endpoints and redistributing the remaining points

are removed, the rest of the points should be redistributed with equal spacing. Figure 4.5 show the axial view of a Francis runner after removing upward curvature at the hub, cutting endpoints and redistributing the remaining points. If constraints exist for the outlet diameter, it has to be checked that the outlet diameter after cutting endpoints does not exceed the limits.

Runner radial view

In order to simplify the design process of going from the axial view to the radial view, a GH-plane is defined. G is the length of a streamline in the axial plane and H is the length of a streamline in the radial plane.

The GH-plane is commonly used when designing centrifugal pump impellers, as described by both Stepanoff [19] and Lazarkiewicz [20].

Calculating the values of G is an easy and straight forward process, using the values of R and Z from the axial view. G equals zero at the inlet.

$$G_{i,1} = G_{i-1,1} + \sqrt{(R_{i-1,1} - R_{i,1})^2 + (Z_{i-1,1} - Z_{i,1})^2} \qquad [m] \tag{4.25}$$

Calculating the values of H is more demanding, as they are dependent on the distribution of the blade angle, β. The blade angle is closely linked to the energy distribution along the blade. The energy distribution is often referred to as the $U \cdot C_u$ distribution, and describes the transformation from pressure energy to rotational energy along the blade. The relation between the energy distribution and the blade angle β is governed by equation 4.26.

$$\beta = \arctan(\frac{C_m}{U - C_u}) \qquad [^\circ] \tag{4.26}$$

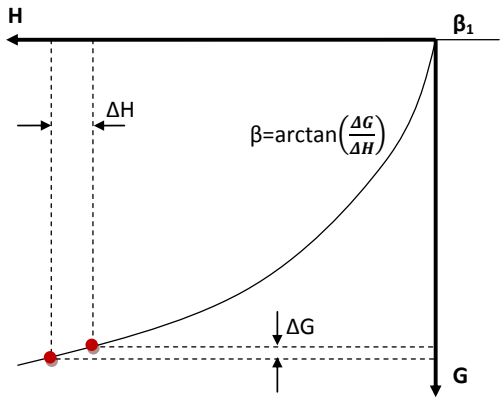

Figure 4.6: Definition of *G-H* plane. Adapted from Eltvik et al. [3]

The blade angles at the inlet and outlet are known from the velocity triangles. The distribution in between has to be determined. This can be done in two ways. Either you can choose the $U \cdot C_u$ distribution and then calculate the β distribution, or you can choose β and then calculate $U \cdot C_u$. Choosing the blade angle distribution gives the designer full control of the design outcome, and avoids any strange designs. Choosing the energy distribution and subsequently calculating the blade angle distribution, you gain the advantage of controlling the energy distribution, but you lose the control of the blade angle, and thus some strange designs may occur. A good practice is to control the corresponding distribution afterwards, either if the energy or the blade angle distribution is chosen. A distribution must be specified for each streamline, but you could of course specify the same distribution for all streamlines. The same $U \cdot C_u$ distribution for all streamlines will give a different distribution of the blade angle for each streamline. Likewise, equal blade angle distribution for all streamlines will give a different energy distribution for each streamline. The corresponding distributions are calculated using equation 4.26.

C_m is the velocity along the streamline, and is found using the continuity equation. The peripheral velocity U is dependent on the radius R and the angular velocity ω and is thus known for each point.

$$U = \omega \cdot R \qquad [m/s] \tag{4.27}$$

Next the values of ΔH can be obtained using equation 4.28, defined as shown in figure 4.6.

$$\Delta H = \frac{\Delta G}{\tan \beta} \qquad [m] \tag{4.28}$$

When this is performed for each streamline, the *G-H* plane can be plotted. The radial view is established using equation 4.29, which is defined according to figure 4.8.

$$d\theta = \frac{\Delta H}{R} \tag{4.29}$$

When knowing all the coordinates for θ and R, the radial view can be plotted as in figure 4.9.

Combining the axial coordinates and the radial coordinates, the 3D shape of the runner blade emerges as shown in figure 4.10.

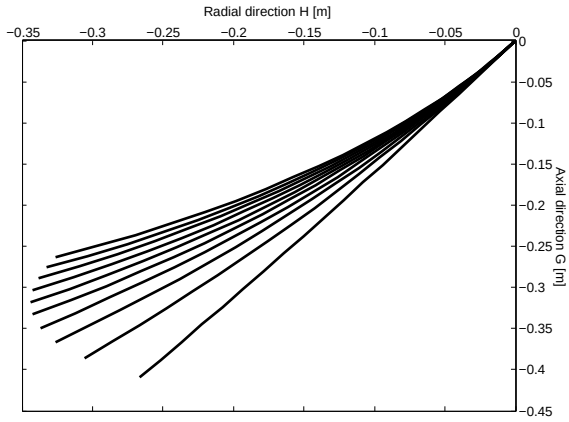

Figure 4.7: GH-plane

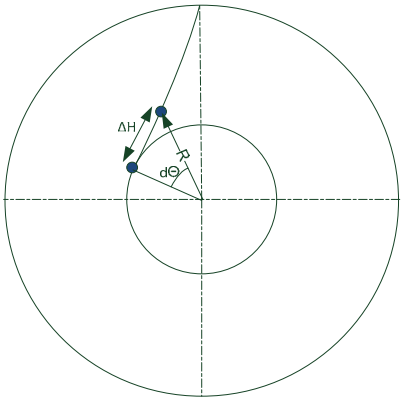

Figure 4.8: Definition of θ

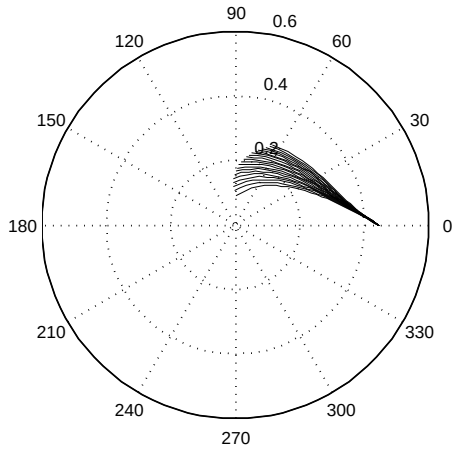

Figure 4.9: Radial view

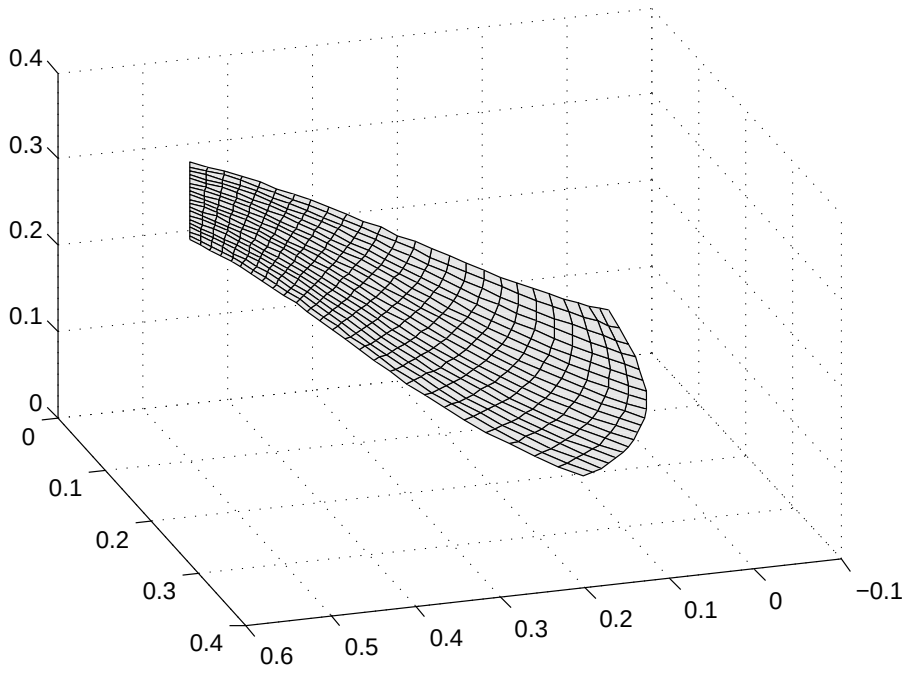

Figure 4.10: 3D-blade plotted without thickness

4.4 Runner

This section presents simplified methods for calculating the required number of blades in the runner and the required runner blade inlet thickness. We have however already guessed both number of blades and thickness at the leading and trailing edges in order to find the effective outlet and inlet areas of the turbine when deciding the main dimensions.

It seems that the method for calculating number of blades is excessively conservative, giving a very high number of blades. Furthermore the calculation of the blade thickness is not suitable for turbines where sediment erosion is expected. Then it makes sense to have thicker blades.

Number of blades in the runner

When the shape of the blade is established, the number of blades in the runner has to be decided. This is done by investigating equation 4.30

$$\frac{\partial w}{\partial n} = -2\omega - \frac{w}{r_{curv}} \qquad [1/s] \tag{4.30}$$

where r_{curv} is the radius of curvature of the blade surface.

The equation is derived from the balance of forces acting on a particle in a rotating channel, and describes the change in relative velocity, w, along a line, n, normal to the streamlines in the channel.

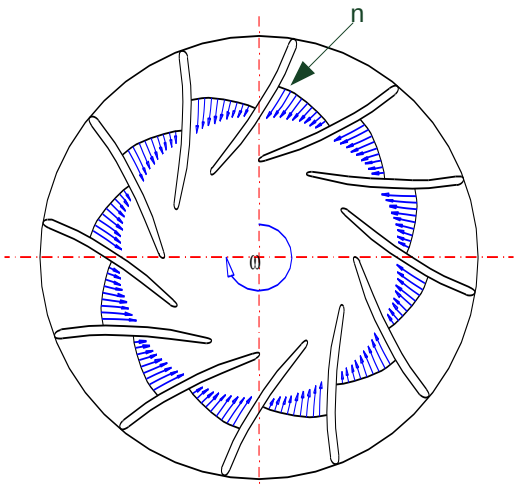

Figure 4.11: Relative velocity in rotating channel [4]

As can be seen from figure 4.11, the lowest relative velocity appears on the pressure side of the blade. To avoid backflow, the relative velocity at the pressure side cannot be negative.

In general, the -2ω term is relatively much larger than the $\frac{w}{r_{curv}}$ term in equation 4.30, and thus we can conclude that the value of $\frac{\partial w}{\partial n}$ will be close to constant. That will give a velocity profile which is almost linear. For calculation purposes, the profile is assumed to be entirely linear.

$$\frac{\partial w}{\partial n} = \frac{\Delta w}{\Delta n} \tag{4.31}$$

Solving for Δn:

$$\Delta n = \frac{1}{\frac{\partial w}{\partial n}} \Delta w = const \cdot \Delta w \tag{4.32}$$

Δn is the distance from the middle of the channel to the blade. The relative velocity increases with the flow rate, and the maximum relative velocity is found at full load, as can be seen in figure 4.12. As a decrease in Δw will cause narrower channels, and consequently an increased number of blades required, the dimensioning case for the number of blades will be found at part load. At some point on part load, backflow has to be allowed, and this limit has to be decided. This is, according to Dahlhaug [25, Personal conversations], typically set to 80 percent of the flow rate at design load.

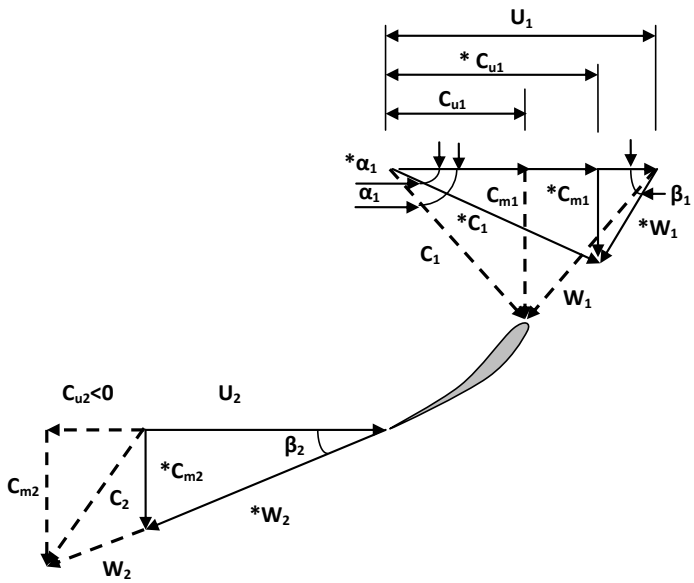

Figure 4.12: Velocity diagram at BEP (*) and at full load

To calculate the least number of blades required to avoid backflow at the inlet, the relative velocity is set to zero at the inlet on the pressure side. The relative velocity in the middle of the channel is calculated based on the flow rate at 80 percent part load, Q_{80}. As the exact behavior of the C_u component is hard to calculate, it is in the design process assumed to obtain the same values as at design load. The peripheral speed is the same as on design load and the C_m component is found from continuity. Thus the relative velocity is found from the velocity triangles, and $\frac{\partial w}{\partial n}$ is calculated from equation 4.30. Next, the distance from the center of the channel to the pressure side, Δn, is found from equation 4.32.

The distance between two blades are $2\Delta n$. The circumference of the runner is known from the main dimensions. Hence the least number of blades to avoid back flow is:

$$Z_{rb} = \frac{\text{Circumference}}{\text{Channel Width}} = \frac{\pi D_1}{2\Delta n} \qquad [-] \tag{4.33}$$

This calculation of number of blades should be checked with CFD analysis, as the blade thickness is not accounted for, and because of the assumption of a linear velocity distribution and the simplification of the behavior of the C_u component. The simplification of the C_u component is discussed in the further work section.

Thickness of blades

After the number of blades in the runner is determined, the thickness of each blade can be calculated. The thickness has to be large enough to withstand the hydraulic forces which the blade is exposed to, being the static pressure difference between the pressure and the suction side of the blade, and the dynamic pressure pulsations.

As the geometry of the runner blades are quite complex, a simplified stress analysis is performed to calculate a conservative estimate of the required blade thickness. Modeling the blade as a straight beam between hub and shroud, classical mechanics is applicable. The hub is considered to be rigid, while the shroud is assumed to be flexible in torsion with respect to the hub. This means that the blade can be modelled as a beam that is clamped at the hub side and guided at the shroud side.

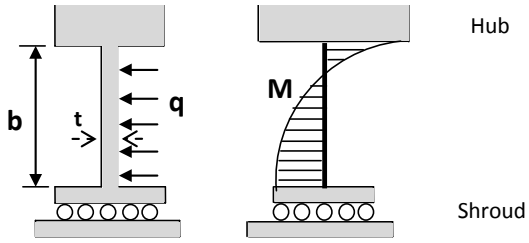

Figure 4.13: Blade modeled as a straight beam between hub and shroud

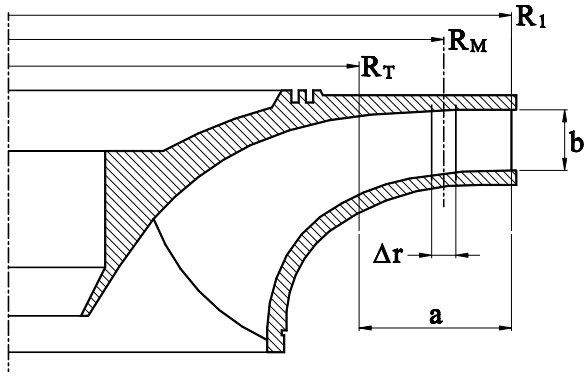

Figure 4.14: Definition of a, b, Δr and R_M

Assuming equally distributed load, $q = \Delta r \Delta p$, the bending moment, M, is found as [26]

$$M = q\frac{b^2}{3} \qquad [Nm] \tag{4.34}$$

The maximum bending stress, σ_{max}, is

$$\sigma_{max} = \frac{M}{I}\frac{t}{2} \qquad [Pa] \tag{4.35}$$

with blade thickness, t, and second area moment of inertia, I

$$I = \frac{\Delta r t^3}{12} \qquad [m^4] \tag{4.36}$$

Rearranging equation 4.34 - 4.36 gives the minimum blade thickness at the inlet as

$$t_{min} = \sqrt{\frac{2b^2\Delta p}{\sigma_{max}}} \qquad [m] \tag{4.37}$$

The pressure difference is calculated from the torque on the runner. The length a defined in figure 4.14, is an imaginary length where it is assumed that the entire torque is transferred from the flow to the blade. The value of a is usually set to 1.5 b according to Brekke [21].

$$M_{runner} = Z_r a b R_M \Delta p = \frac{P}{\omega} \qquad [Nm] \tag{4.38}$$

$$\Delta p = \frac{P}{Z_r a b R_M \omega} \qquad [Pa] \tag{4.39}$$

4.5 Leading and trailing edge

The shape of the leading and trailing edge are designed based on experience as shown in figure 4.15 [27, personal conversation]. The trailing edge shape is chosen in order to minimize the amplitude of von Karman vortices.

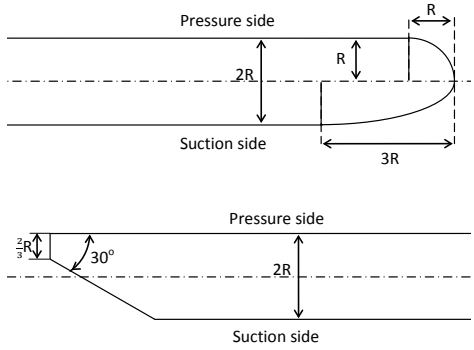

Figure 4.15: Shape of leading and trailing edge

4.6 Guide vanes

A number of adjustable blades, known as guide vanes, govern the discharge and the direction of the flow before it enters the runner.

The number of guide vanes has to be chosen. To minimize the extent of the pressure pulsations that occur when the runner vanes pass the guide vanes, the number of guide vanes has conform to equation 4.40.

$$\frac{\text{Number of Guide vanes}}{\text{Number of Runner vanes}} \neq \text{Integer} \tag{4.40}$$

To have sufficient distance between the guide vane and the runner, it is common to design the guide vanes outlet diameter at rated power approximately five percent larger than the runner inlet diameter. The gap between the guide vane outlet and the runner inlet is less at full power, and it should be controlled that there is sufficient clearance also at this guide vane position.

As flow in the gap between the guide vane outlet and the runner inlet is unaffected, the free vortex theory is used to find the tangential component of the absolute velocity at the trailing edge of the guide vanes.

$$C_{u1} r_1 = C_{ugvo} r_{gvo} = \text{Constant} \tag{4.41}$$

The meridional component is found using continuity and the guide vane outlet angle is found from the velocity triangle.

$$\tan \alpha_{gvo} = \frac{C_{mgvo}}{C_{ugvo}} \qquad [-] \tag{4.42}$$

Next, the radial position of the guide vane axis, r_0, has to be determined. When r_0 is known, the length from the trailing edge to the axis of the guide vane, L_0, is found from the law of cosine.

The length of the guide vane is dependent on the number of vanes, as the vanes have to overlap in the closed position. This is to avoid the vane from being able to rotate full circle. It is common to have an overlap with a cover factor, K_{cf}, of approximately 10 - 15 percent [3]. With few vanes, each vane has to be longer. A long vane guides the flow better than a short one, but it also accounts for larger friction losses. Thus the choice of number of guide vanes should be carefully considered.

$$L_{gv} = \frac{\pi D_0 K_{cf}}{Z_{gv}} \qquad [m] \tag{4.43}$$

The guide vane axis should be located somewhere between the middle and three quarters of the vane length upstream from the trailing edge. It is important that both the overlap and axis location criteria are satisfied. The guide vane inlet diameter can now be found using the law of cosine.

To decrease the flow losses in the guide vane cascade, it is desirable to shape the vane as an airfoil. Smooth and symmetrical NACA profiles are often chosen.

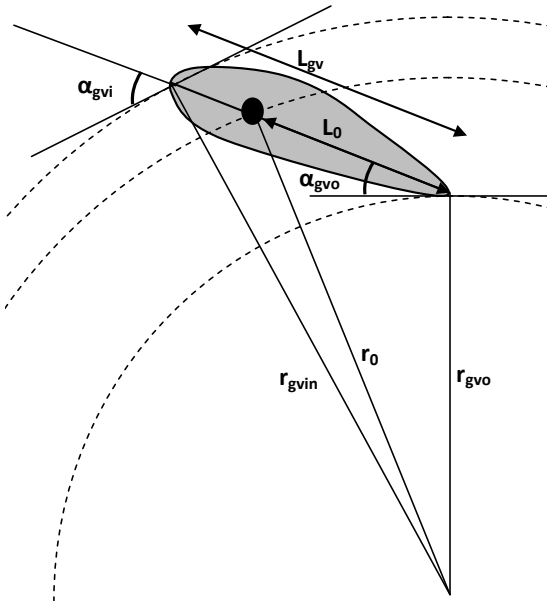

Figure 4.16: Geometry of guide vane

4.7 Stay vanes

The stay vanes are designed to have no hydraulic effect, and are present in the turbine cascade just to keep the spiral casing together. Thus the stay vanes have to withstand the maximum hydraulic force acting on the spiral casing.

The shape of the stay vanes follows a free vortex. The outlet diameter is usually chosen 2 percent larger than the guide vane inlet diameter [3]. The design process requires the designer to choose a stay vane inlet diameter. Then the length of the vane can be found, as the length of a streamline following the path of the free vortex from stay vane inlet to stay vane outlet.

The maximum force acting on the spiral casing is the maximum pressure times the area on which the pressure acts. The effective area of the spiral casing and the stay vanes is difficult to determine. As a simplification, the spiral casing and the stay vanes are modeled as an annulus with constant inner and outer diameter.

$$F_{max} = p_{max} \cdot A_{annulus} \qquad [N] \tag{4.44}$$

$$A_{annulus} = \frac{1}{4}\pi(D^2_{outer} - D^2_{inner}) \qquad [m^2] \tag{4.45}$$

The maximum pressure acting on the area of the spiral casing occurs if the turbine running at full power is suddenly shut down. This will cause large pressure pulsations, known as the water hammer. The water hammer and the static pressure

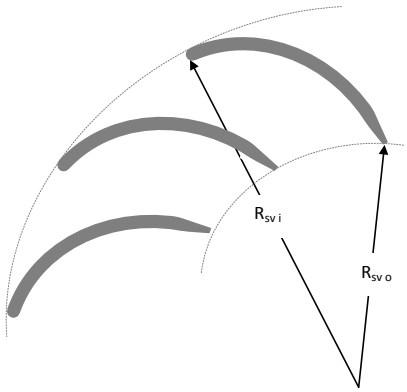

Figure 4.17: Stay vanes

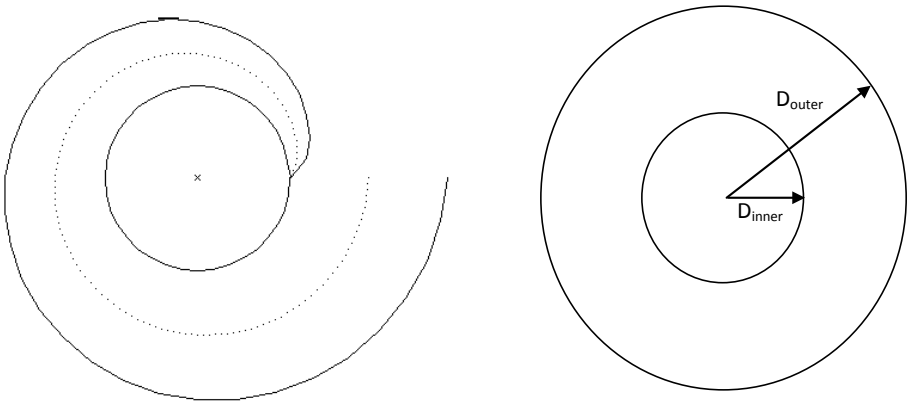

Figure 4.18: Traditional spiral casing and simplified annulus for calculating purposes

caused by the head difference give the dimensioning pressure.

$$p_{max} = p_{head} + p_{waterhammer} \qquad [Pa] \tag{4.46}$$

Then the required cross sectional area of the stay vane can be found with maximum bending stress for steel, σ_{max}, equal to 100 MPa. Subsequently the required thickness is calculated.

$$A_{required} = \frac{F_{max}}{\sigma_{max} Z_{sv}} \qquad [m^2] \tag{4.47}$$

$$t_{sv} = \frac{A_{required}}{L_{sv}} \qquad [m] \tag{4.48}$$

4.8 Spiral casing

The purpose of the spiral casing is to distribute the flow evenly around the runner. Thus the cross section area of the spiral casing has to decrease downstream, as parts of the water flows through the stay vanes in each section.

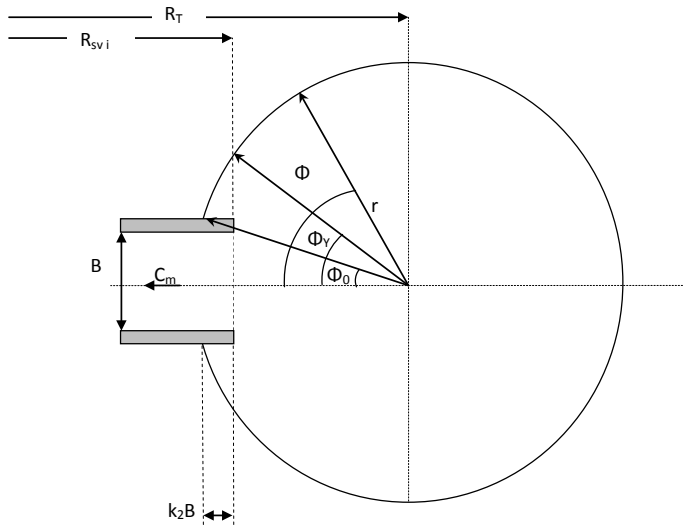

Figure 4.19: Cross section of spiral casing

The boundary layer in the spiral casing cause an energy loss, but it also induce a secondary flow. To prevent this secondary flow to propagate into the stay vanes and guide vanes, the spiral casing overlaps the stay vane inlet. The overlap factor

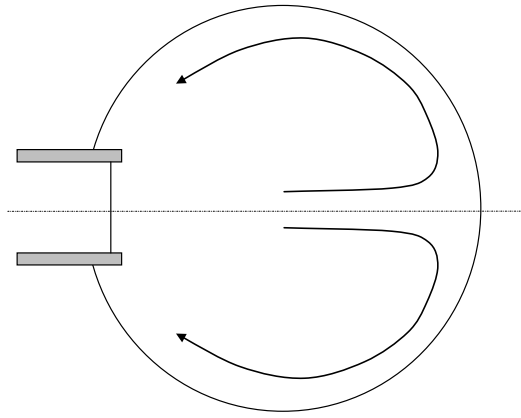

Figure 4.20: Secondary flow in the spiral casing

K_2 is traditionally set to 0.1 for high head Francis turbines [21]. For the design software however, this factor has been set to 0.05 based on discussions in the weekly design team meeting [28].

When designing the stay vanes, the designer has to choose a stay vane inlet radius, R_{svi}. As it is desirable to minimize the flow losses in the spiral casing, the casing is designed so that the flow follows a free vortex. The free vortex constant, K_{FV}, is found from the inlet dimensions of the stay vanes.

$$K_{FV} = C_{usvi} R_{svi} \qquad [m^2/s] \tag{4.49}$$

The spiral casing is made of a number of sections chosen by the designer. Many sections cause a better and more correct reduction of the flow through the spiral casing, but it is also more expensive to manufacture due to the increased number of weld joints.

R_T and r has to be calculated for each section in order to find the cross section area. This is obtained by at first choosing a starting value of r. Then ϕ_0 and ϕ_y is calculated from geometrical relations according to figure 4.19. Next, R_T is calculated from equation 4.50, and then an new value of r is found by solving equation 4.51 with respect to r. This is an iterative process, which is repeated until the value of r has converged.

$$R_T(\theta) = R_{svi} + r(\theta) \cdot \cos(\phi_0) - K_2 B \qquad [m] \tag{4.50}$$

$$Q(\theta) = 2r(\theta)^2 K_{FV} \int_{\phi_y}^{\pi} \frac{\sin^2(\phi)}{R_T(\theta) - r(\theta) \cdot cos(\phi)} d\phi \qquad [m^3/s] \tag{4.51}$$

When the dimensions of the spiral casing have been found, the thickness of the stay vanes should be calculated. If the required thickness is too small or too large, a new stay vane inlet diameter should be chosen. Subsequently the calculations of stay vane length, spiral casing dimensions and required stay vane thickness should be performed over again. This should be repeated until the required thickness of the stay vanes is acceptable.

B CFD

The CFD analysis was performed by using Ansys CFX 13.0. Mesh was made using TurboGrid. The simulations were run i batch-mode from Matlab. This chapter will give further background information behind CFD and turbulence modelling.

B.1 Basic equations

Fluid dynamics is based on the three fundamental principles of Newtons 2. law, mass conservation and energy conservation. These equations are solved as partial differential equations in the CFD solver as they are difficult to solve analytically.

The Continuity Equation:

$$\frac{\partial \rho}{\partial t} + \Delta(\rho U) = 0 \tag{B.1}$$

The Momentum Equations:

$$\frac{\partial \rho U}{\partial t} + \Delta(\rho U \cdot U) = -\Delta p + \Delta \cdot \tau + S_M \tag{B.2}$$

where τ is the stress tensor and S_M is the momentum source. The total Energy Equation:

$$\frac{\partial \rho h_{tot}}{\partial t} - \frac{\partial \rho}{\partial t} + \Delta(\rho U \cdot h_{tot}) = \Delta(\lambda \Delta T) + \Delta(U \cdot \tau) + U \cdot S_M + S_E \tag{B.3}$$

where h_{tot} is the total enthalpy, $\Delta(U \cdot \tau)$ is the viscous term, $U \cdot S_M$ is work due to external momentum sources awhich are neglegted and S_E is the energy source.

C View of Khoj

The Matlab code for the design software is found in the folder *Design Software* on the attached CD or zipped folder.

The program is run by executing the file named RunMe.

New versions of the program are expected.

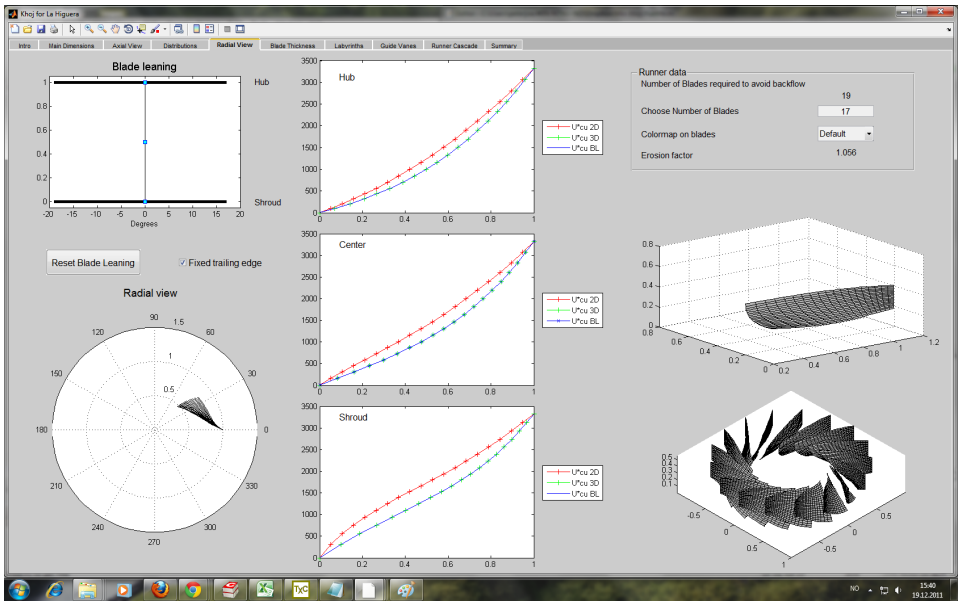

Figure C.1: Tab 5 - Radial view of runner blade. The new blade leaning parameter is visible in the upper left corner. The graphs in the center displays change in energy distribution when blade leaning is introduced.

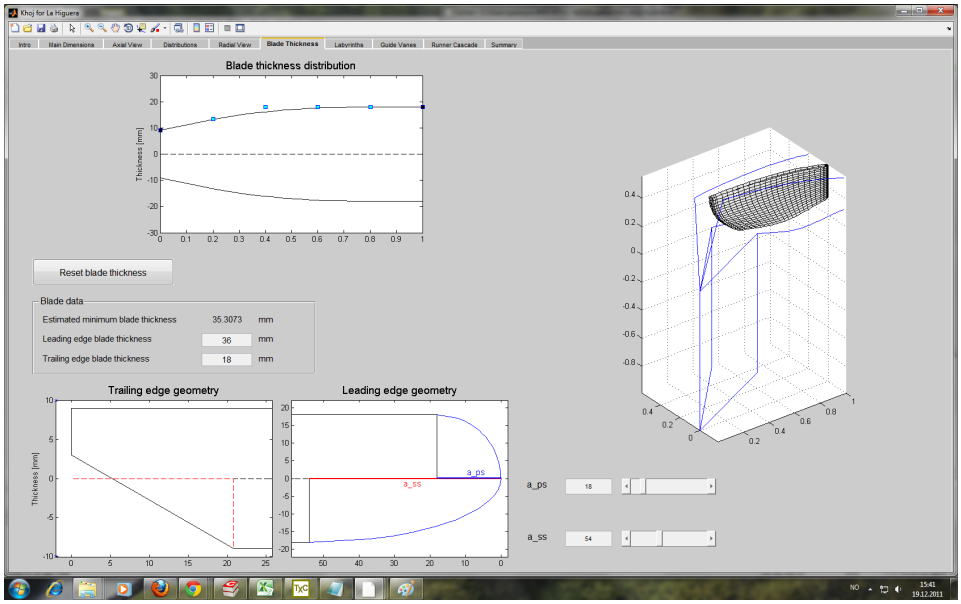

Figure C.2: Tab 6 - Blade thickness. In the upper left corner, the blade thickness distribution is displayed. At the bottom, the trailing and leading edge shape is displayed
fig:tab6

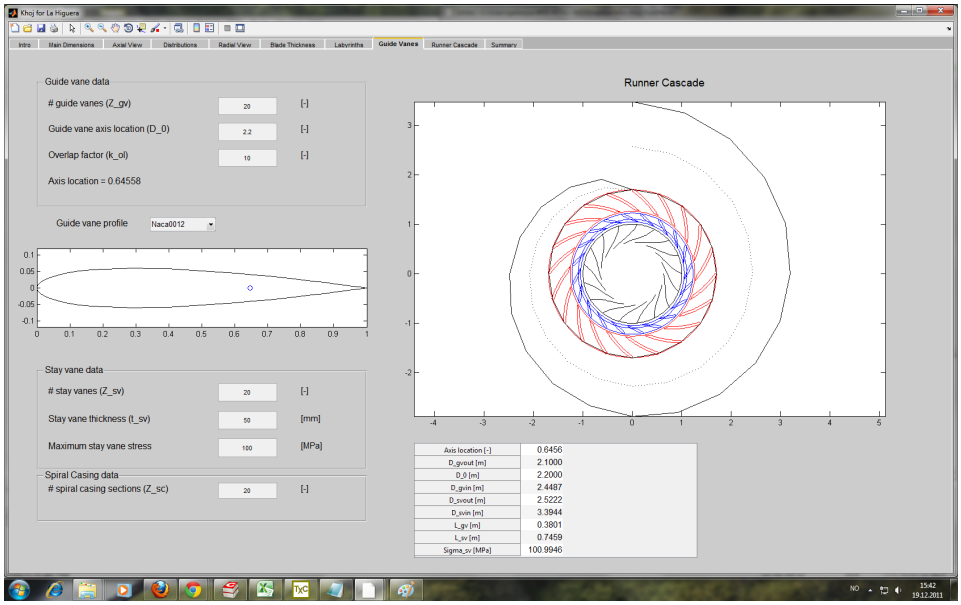

Figure C.3: Tab 8 - Guide Vanes. This tab displays the runner cascade in 2D. Tha shape of the leading edge is shown in the figure to the left. The different parameters are sorted

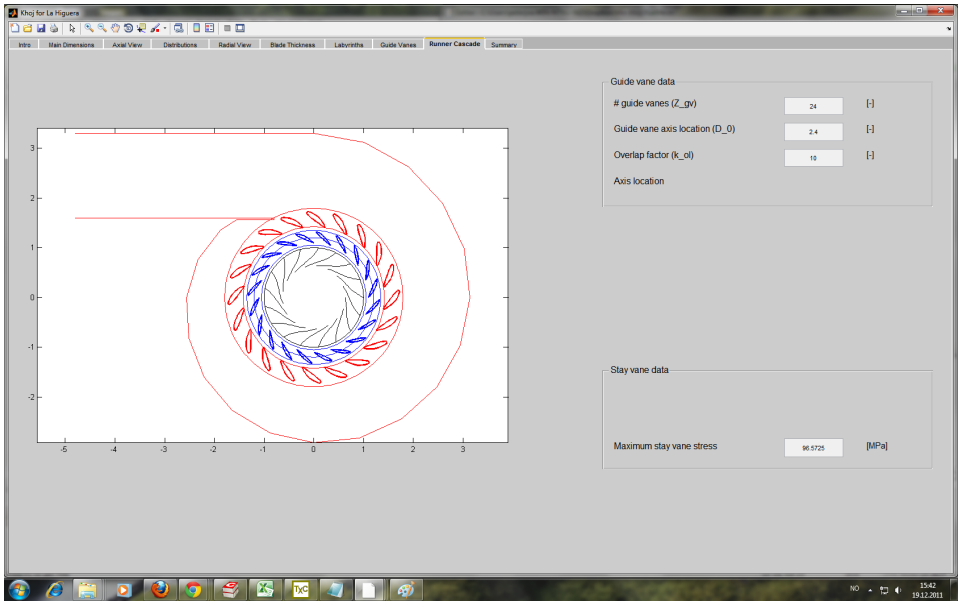

Figure C.4: Tab 9 - Runner cascade. Currently this tab i displaying the runner, guide vanes and stay vanes for La Higuera. It will be developed to show the runner cascade in 3D